Challenge Journal of STRUCTURAL MECHANICS

Vol.6 No.2 (2020)

Mindlin's theory buckling building codes compressive strength dynamic analysis dynamic response earthquake finite element analysis finite element method mechanical properties nonlinear analysis optimization prefabrication pushover analysis reinforced concrete seismic analysis seismic design seismic isolation shallow foundations steel silo temperature effects thick plate wind

ISSN 2149-8024

TULPAR ACADEMIC PUBLISHING

Challenge Journal of Structural Mechanics

E-mail: *cjsmec@challengejournal.com*

Web page: *cjsmec.challengejournal.com*

TULPAR Academic Publishing
www.tulparpublishing.com

Challenge Journal of Structural Mechanics

CONTENTS

Research Articles

TULPAR ACADEMIC PUBLISHING

Challenge Journal of Structural Mechanics

Research Article

A study on seismic isolation of building used LRB

Muhammet Yurdakul [a,*], Mehmet Burak Yıldız [a]

[a] *Department of Civil Engineering, Bayburt University, 69000 Bayburt, Turkey*

ABSTRACT

Base isolation system with lead rubber bearing (LRB) is commonly used to prevent structure against to damage of earthquake. Design of LRB system is detailed in this study. The isolated building with LRB design according to Uniform Building Code (UBC-97) and fixed building were examined. The six-storey building with LRB and fixed building were modelled in SAP2000 with the same dynamic loads. The relative floor displacement and internal forces of the seismic isolated and fixed building are compared. In addition, transverse and longitudinal reinforcement of any axis of seismic isolated and fixed building are compared. Analyse results showed that effectiveness of using seismic isolation system on building. The weight of longitudinal and transverse reinforcement of isolated building is smaller than fixed building about 36%, 40% respectively.

ARTICLE INFO

Article history:
Received 7 November 2019
Revised 25 December 2019
Accepted 8 January 2020

Keywords:
Base isolation
Lead rubber bearing
Dynamic analysis
Isolator design

1. Introduction

Earthquake is inevitable natural disaster which occurs unknown time and place. Detrimental effects of earthquake on building and decreasing these effects are most important issues in the world. There is some way to decrease these effects. Base isolation system is one of them. Use of base isolation system is decrease lateral load of earthquake. This give rise to less internal forces. So, smaller size elements and reinforcement are sufficed.

Base isolation systems basically are separated two types as sliding and rubber isolation system. The laminated rubber bearing system is commonly used isolation system among rubber isolation systems. There are several studies on effectiveness of LRB system in literature. Su et al. (1989) carried out a comparative study of effectiveness of various base isolation systems. One of them is laminated rubber bearing. Analyses results show that base isolators can significantly reduce the acceleration transmitted to the superstructure. Tavakoli et al. (2015) evaluated the effect of LRB system to increase the resistance of structures against progressive collapse. Authors used concrete moment resisting frames in both the fixed and base isolated model structures. The analyses results showed that push down analysis is dependent on location of removal column and floor number of buildings. Liu et al. (2016) carried out a study of seismic isolation performance of prestressed concrete (PC) continuous beam bridge using lead rubber bearings. It was pointed out that use of rubber isolation system can effectively reduce the seismic damage to the bridge. Abadi and Adhami (2016) carried out improving the seismic behaviour of symmetrical steel structures under near field earthquake using a base isolation system with LRB isolator. The analysis results point out a significant reduce in the results of base shear, the acceleration and floors drift in the seismically isolated system in comparison with the fixed base structure. Nakhostin and Poursha (2017) attempted to extend the modal pushover analysis and the extended N2 (EN2) method to medium-rise base-isolated building frames with LRB to account for the effect of higher modes in predicting the seismic demands of these structures. It was observed from analyses results that N2 method with the PSC load distribution gives better estimates of the seismic demands for low rise base isolated frames. Reddy et al. (2017) examined effect of base isolation with LRB in multi-storeyed reinforced concrete building. Analysis results showed that period of the isolated structure longer than that of fixed structure. Base shear is significantly reduced as compared to fixed structure by using the isolators. Wu et al. (2018) conducted a study included compression shear properties of

* *Corresponding author*. Tel.: +90-458-211-1152 ; Fax: +90-458-211-1178 ; E-mail address: myurdakul@bayburt.edu.tr (M. Yurdakul)
ISSN: 2149-8024 / DOI: https://doi.org/10.20528/cjsmec.2020.02.001

small size seismic isolation rubber bearings. Analyse results show that all the research methods can reveal the fundamental properties of the small size bearings. Tanwer et al. (2018) studied on different types of base isolation system over fixed based. Dynamic behaviour of seismic isolated with LRB and fixed were investigated. Habieb et al. (2019) compared fixed and isolated a masonry building with fiber reinforced elastomeric isolators. The study showed that the isolation system significantly reducing the damage level of the masonry building. Kumar and Petwala (2019) carried out a study included comparing of secondary system of isolated and fixed building. The analyses results showed that the base isolated building gives better performance. Shoaei and Mahsuli (2019) puts forward an approach to seismic design of isolated steel moment frame structures with LRB devices. The proposed approach is showcased for an example steel moment frame structure. Billah and Todorov (2019) evaluated the seismic performance of a base isolated bridge with LRB at subfreezing temperature. Analysis results point out that freezing condition may have a remarkably effect on the component fragility. There is a study to develop software for designing of steel reinforced elastomeric isolator according to American Association for State Highway and Transportation Officials Load and Resistance Factor Design (Atmaca and Ateş, 2017).

In generally, LRB system is used as an isolation device on building to against harmful of earthquake ground motion. There is no detailed study involving the design of LRB isolation system in the literature. This study may able to close this gap. Also, the cost efficiency of LRB system is investigated.

2. Material and Method

LRB bearing system was designed for Uniform Building Code (UBC-97) (Atmaca and Ateş, 2017) and used for seismic isolation system in this study. The UBC-97 regulation is based on the assumption that the displacement remains at the base isolation level and that the superstructure behaves rigidly. Therefore, the first vibration mode is important according to this regulation. UBC-97 is obliged to spectral analysis when the building was constructed on weak ground types of the building, the period of building is longer than 3 sec. under the maximum earthquake load and building height is higher than four floors or higher than 19.8 m. It is assumed that the selected building was built in Istanbul. Response spectrum analyses is carried out in SAP2000 (Atmaca and Ateş, 2017).

2.1. Selecting parameters to be used in UBC-97

Seismic isolator was used in the 1st earthquake zone in UBC-97. Effective ground acceleration, A_o, is 0.4. Therefore, seismic zone factor (Z) is selected as 4 from Table 1. Istanbul is located on zone 4 according to UBC-97.

It is assumed that selected building was built hard rock. The floor profile type is selected as S_A from Table 2.

Table 1. Seismic zone factor (UBC-97).

Zone	1	2A	2B	3	4
Z	0.075	0.15	0.20	0.30	0.40

Table 2. Soil profile type (UBC-97).

Soil Profile Type	Soil Profile Name/Generic Description	Average soil properties for top 100 feet (30 480 Mm) of soil profile		
		Shear Wave Velocity $\bar{v}_s$(m/s) feet/second (m/s)	Standard Penetration Test, $\bar{N}$ [or $\bar{N}_{CH}$ for cohesionless soil layers] (blows/foot)	Undrained Shear Strength $\bar{s}_u$ psf (kPa)
S_A	Hard Rock	>1500	-	-
S_B	Rock	760-1500	-	-
S_C	Very Dense Soil and Soft Rock	360-760	>50	>100
S_D	Stiff Soil Profile	180-360	15-50	50-100
S_E	Soft Soil Profile	<180	<15	<50
S_F	Soil Requiring Site-specific Evaluation.			

In UBC-97, seismic source type is classified as A, B and C according to the seismic risk of the fault lines. It is assumed that selected building was located in the first earthquake zone and close to the faults that may cause major earthquakes. So seismic source type A is selected from Table 3.

Since it is assumed to be distance to seismic source less than 2 km and seismic source type is A, near source factor (N_V) is selected as 2.0 from Table 4.

Seismic zone factor (Z), soil profile type and near source factor are selected as 0.4, S_A and 2, respectively. With these values, $0.32N_V$ is selected from Table 5. Since N_V is equal to 2, seismic coefficient (C_v) is calculated as 0.64.

Isolators with damping ratio of 10% are selected and damping coefficient is determined as 1.2 from Table 6.

Since the structural system of the building to which the isolation is to be applied is the frame system which transfers moment, Coefficient of Structural System Behaviour (R) coefficient is selected from Table 7.

Table 3. Soil source types (UBC-97).

Seismic Source Type	Seismic Source Description	Seismic Source Definition	
		Maximum Moment Magnitude (M)	Slip Rate, SR (mm/year)
A	Faults that are capable of producing large magnitude events and that have a high rate of seismic activity	M ≥ 7.0	SR ≥ 5
B	All faults other than Types A and C	M ≥ 7.0 M < 7.0 M ≥ 6.5	SR < 5 SR > 2 SR < 2
C	Faults that are not capable of producing large magnitude earthquakes and that have a relatively low rate of seismic activity	M < 6.5	SR ≤ 2

Table 4. Near source factor (UBC-97).

Seismic Source Type	Closest Distance to Known Seismic Source			
	≤ 2 km	5 km	10 km	≥ 15 km
A	2.0	1.6	1.2	1.0
B	1.6	1.2	1.0	1.0
C	1.0	1.0	1.0	1.0

Table 5. Seismic coefficient (UBC-97).

Seismic Source Type	Seismic Zone Factor (Z)				
	Z=0.075	Z=0.15	Z=0.2	Z=0.3	Z=0.4
S_A	0.06	0.12	0.16	0.24	0.32 N_V
S_B	0.08	0.15	0.20	0.30	0.40 N_V
S_C	0.13	0.25	0.32	0.45	0.56 N_V
S_D	0.18	0.32	0.40	0.54	0.64 N_V
S_E	0.26	0.50	0.64	0.84	0.96 N_V
S_F	Site-specific geotechnical investigation and dynamic site response analysis shall be performed to determine seismic coefficients for Soil Profile Type S_F				

Table 6. Damping coefficient (UBC-97).

Effective Damping (β_D, β_M)	(B_D, B_M)
≤ 2	0.8
5	1.0
10	1.2
20	1.5
30	1.7
40	1.9
≥ 50	2.0

Table 7. Coefficient of structural system behaviour (UBC-97).

Structural system	R_1	R
Frame transferred moment	2	8.5
Shear wall	2	5.5
Concentrically braced frame	1.6	5.6
Eccentrically braced frame	2	7

2.2. Building information to be used in design

Selected building to examine is given Fig. 1. The first vibration of the 6-storey building was determined as 0.6 sec. Targeted period is 1.8 sec. Two different LRB isolator are used in this study. These are type A and type B. Type A is supported 680 kN axial load and shear modulus is 0.65 MPa. 16 pieces of type A isolator were used in building. Type B is supported 1150 kN axial load and shear modulus is 1.00 MPa. 8 pieces of type B isolator were used in building. The total weight of the building (g + 0,3q) is 18700 kN.

2.3. Design of LRB

2.3.1. The minimum horizontal stiffness

The minimum horizontal stiffness, k_D, is calculated by Eq. (1) according to UBC-97.

$$k_D = \frac{4\pi^2 \times W}{T_D^2 \times g} \quad (1)$$

where k_D is the minimum horizontal stiffness, W is axial load supported by isolator, T_D is target period and g is gravity acceleration. Minimum horizontal stiffness was calculated as 0.845 MN/m and 1.428 MN/m for type A and type B isolator by Eq. (1).

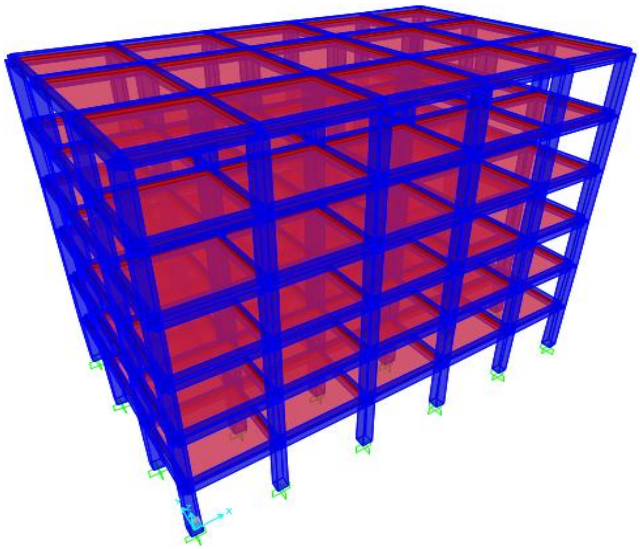

Fig. 1. 3D finite element model of the building used in the study.

2.3.2. Design displacement

The maximum displacement is calculated by Eq. (2).

$$D_D = \frac{g \times C_{vD} \times T_D}{B \times 4\pi^2} \tag{2}$$

where D_D is displacement, C_{VD} is coefficient of seismic and B is damping coefficient of isolator. Maximum displacement was calculated as 0.239 m by Eq. (2).

2.3.3. Calculation of isolator thickness

Isolators can make deformation up to 150% of its thickness. So thickness of isolator is calculated by Eq. (3).

$$t_r = \frac{D_D}{\gamma} \tag{3}$$

where t_r is thickness of isolator and γ is deformation coefficient of isolator. Thickness of isolator was calculated 0.2 m by Eq. (3).

2.3.4. Maximum displacement

It is the maximum displacement of the isolator due to torsion. It is calculated by Eqs. (4-6).

$$E = 0{,}05 \times e \tag{4}$$

$$D_{total} = D_D\left(1 - \frac{12 \times E}{b^2 + d^2}\right) \tag{5}$$

$$D_{total} \geq D_D \times 1{,}1 \tag{6}$$

where e is the longest length of the building plan, b and d are the dimensions of the building in the x and y direction. Maximum displacement was calculated as 0.22 by Eqs. (4-6).

2.3.5. Base shear force

Base shear force of the isolated building is calculated by Eqs. (7-9).

$$V_b = K_H \times D_D \tag{7}$$

$$V_s = \frac{K_H \times D_D}{R} \tag{8}$$

$$C_s = \frac{V_S}{W_T} \tag{9}$$

in which V_b is unreduced earthquake force, V_s is base shear force, R is earthquake reduction coefficient and C_s is the ratio of base shear force to building weight. Base shear force was calculated as 3.08 MN by Eqs. (7-8). The ratio of base shear force to building weight was calculated as 16.5% by Eq. (9).

2.3.6. Detail of lead rubber isolator

In UBC-97, a steel plate thickness to be placed between the elastomer layers was made as 2 mm in standards. The thickness of one of the layers in the isolator is calculated by Eq. (10) and the shape factor of the isolator calculated by Eq. (11).

$$\frac{D}{80} \leq t_0 \leq \frac{D}{40} \tag{10}$$

$$S = \frac{\text{Disc area}}{\text{Cross section area}} = \frac{\frac{R \times D^2}{4}}{R \times D \times t} = \frac{D}{4 \times t} \tag{11}$$

where t_0 is the thickness of the rubber between the steel plates and S is the shape factor of the isolator.

The thickness of the elastomer layers between the isolator was calculated as 10 mm by equation 10, the shape factors of type A and type B were calculated as 15 and 16.25, respectively.

The total elastomer thickness was calculated as 200 mm, one-layer elastomer thickness was calculated as 10 mm, and there are 20 layers of elastomer. There are 19 steel plates with a thickness of 2 mm. There are 25 mm steel plates on the top and bottom of the isolators. Total isolators height was calculated as 288 mm. Type A and type B isolators are given Figs. 2 and 3, respectively.

2.3.7. Vertical stiffness

The loading module is calculated by Eq. (12) and vertical stiffness is calculated by Eq. (13).

$$E_C{}^A = \frac{6 \times G_A \times S_A{}^2 \times K}{6 \times G_A \times S_A{}^2 + K} \tag{12}$$

$$K_V{}^A = \frac{E_C{}^A \times A}{t_r} \quad (13)$$

where E_c, K_v *and* K are loading module, vertical stiffness and stiffness of steel plate, respectively. The stiffness of steel plate is 200 MPa. The loading module of type A and type B isolators are calculated as 609.9 MPa and 884.05 MPa respectively. The vertical stiffness of type A and type B isolators are calculated as 863.01 MPa and 1467.53 MPa respectively. Total stiffness of all isolators is calculated by Eq. (14).

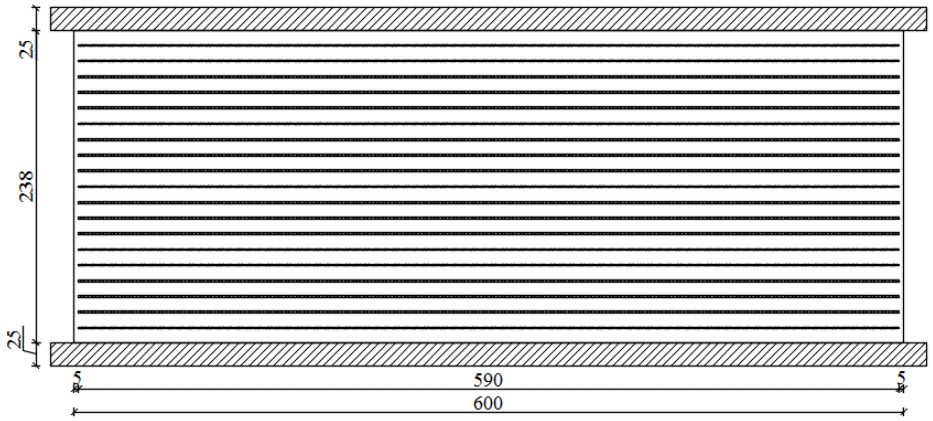

Fig. 2. Detail of type A isolator.

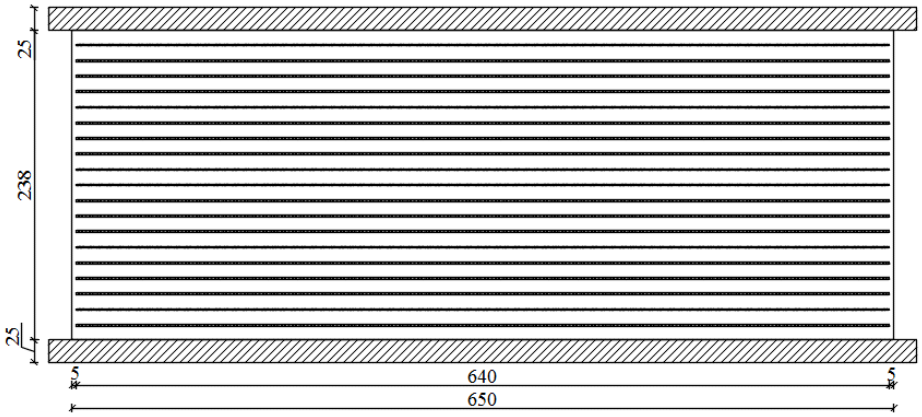

Fig. 3. Detail of type B isolator.

$$\sum K_V = N_A \times N_A{}^V + N_B \times K_B{}^V \quad (14)$$

Total vertical stiffness is calculated as 480829,2 MPa by Eq. (14).

2.3.8. Vertical vibration period

The design displacement of the building is calculated by Eq. (15) and the vertical vibration period is calculated by Eq. (16).

$$\Delta_t = \frac{W_t}{K_V} \quad (15)$$

$$T_V = \frac{T_{DV}}{\sqrt{6S}} \quad (16)$$

where Δ_t is horizontal displacement and T_V is vertical vibration period. The horizontal displacement is calculated as 0.000501 m by Eq. (15) and the vertical vibration period is calculated as 0.17 sec. by Eq. (16).

2.3.9. Control of collapse risk

The inertia of the steel plates of isolator is calculated by Eq. (17) and control of collapse risk is calculated by Eq. (18).

$$I = \frac{\pi \times \left(\frac{D}{2}\right)^2}{4} \quad (17)$$

$$P_{critic} = \frac{\pi}{t_r}\sqrt{\frac{E_C \times I}{3} \times G \times A_S} \quad (18)$$

where P_{critic} is load supported by isolator, I inertia of steel plate. Steel plate inertia for type A and type B isolator is calculated 17 as 0.0059 m^4 and 0.0082 m^4 respectively. P_{critic} for type A and type B isolator is calculated as 7250 kN and 13860 kN respectively. Since the values obtained from calculation are higher than the load supported isolator, there is no collapse risk.

2.3.10. Mechanical properties of isolator

Plastic stiffness is calculated by Eq. (19) and elastic stiffness is calculated by Eq. (20).

$$K_2 = \frac{A \times G}{t_r} \tag{19}$$

$$K_1 = 6 \times K_2 \tag{20}$$

where K_2 is plastic stiffness and K_1 is elastic stiffness. Plastic stiffness for type A and type B is calculated as 0.919 MPa and 1.66 MPa respectively. Elastic stiffness for type A and type B is calculated as 5.514 MPa and 9.96 MPa respectively. Shear force of isolator is calculated by Eq. (21).

$$Q = C_S \times W \tag{21}$$

Shear force of type A and type B is calculated as 0.1122 MPa and 0.1898 MPa respectively.

Yielding displacement is calculated by Eq. (22).

$$D_Y = \frac{Q}{K_1 - K_2} \tag{22}$$

where D_y is yielding displacement. The yielding displacement for type A and type B is calculated as 0,0239m and 0,0229 m respectively.

Effective stiffness is calculated by Eq. (23).

$$K_{eff} = K_1 + \frac{Q}{D} \tag{23}$$

where K_{eff} is equivalent stiffness corresponding to the maximum displacement. K_{eff} for type A and type B is calculated as 1392.04 kN/m and 2475.65 kN/m respectively.

Yielding strength is calculated by Eq. (24).

$$F_y = K_1 \times D_y \tag{24}$$

where F_y is yielding strength. Yielding strength for type A and B is calculated as 129.30 kN and 213.96 kN respectively. Mechanical properties of type A and type B isolator are shown in Table 8.

Table 8. Mechanical properties of isolators.

Direction		LRB			
		Type A (680 kN)		Type B (1150 kN)	
		Linear	Nonlinear	Linear	Nonlinear
U_1 (Vertical)	Stiffness (kN/m)	846612.81	-	1439646.93	-
U_2/U_3 (Horizontal)	Stiffness (kN/m)	1392.4	5409.23	2478	9770.76
	Yielding stiffness (kN)	-	129.3	-	213.96
	K_2 / K_1	-	0.1667	-	0.1667

3. Results

In this study, the internal forces of 6-6 axis of seismic isolated building with LRB and fixed building are compared. As a result of the analyses, the maximum shear forces and moments of the 6-6 axes of the isolated and fixed building are shown in Tables 9-10. 6-6 axis view of the building is shown in Fig. 4.

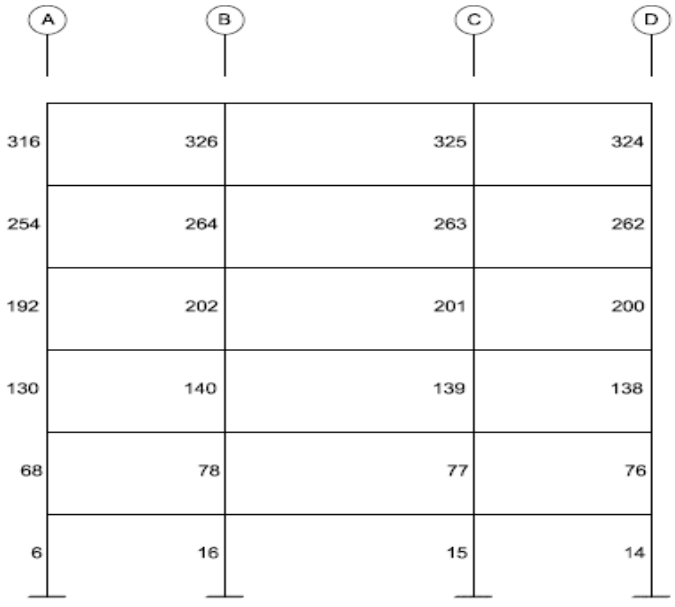

Fig. 4. The view of 6-6 axis of the building.

Table 9. 6-6 Axis column of internal forces of fixed building.

Frame Text	Step Type	V_2 kN	V_3 kN	M_2 kNm	M_3 kNm
6	Max	135.27	126.52	293.09	300.10
6	Min	-126.96	-134.74	-300.98	-292.11
14	Max	135.27	135.27	300.98	300.10
14	Min	-126.96	-126.96	-293.09	-292.11
15	Max	145.22	166.66	331.68	309.66
15	Min	-133.30	-162.58	-327.76	-298.21
16	Max	145.22	162.58	327.76	309.66
16	Min	-133.30	-166.66	-331.68	-298.22

Table 10. 6-6 Axis column of internal forces of isolated building.

Frame Text	Step Type	V_2 kN	V_3 kN	M_2 kNm	M_3 kNm
6	Max	82.13	81.15	245.44	244.42
6	Min	-81.47	-81.81	-243.46	-246.39
14	Max	82.13	82.13	243.47	244.42
14	Min	-81.47	-81.47	-245.44	-246.39
15	Max	82.72	83.92	250.77	245.94
15	Min	-81.98	-83.59	-251.78	-248.16
16	Max	82.72	83.59	251.78	245.94
16	Min	-81.98	-83.93	-250.77	-248.16

The base shear forces of the design earthquakes acting in E_x and E_y directions of the isolated and fixed structure are given in Table 11.

Table 11. Base shear forces of isolated and fixed building.

	Fixed Building	Isolated Building
Ex	4450.65 kN	2542.91 kN
Ey	4420.87 kN	2525.43 kN

The displacement of the floors as a result of the design earthquake affecting the E_x and E_y directions of the fixed and isolated building is given in Table 12.

Table 12. Story displacement of isolated and fixed building.

	Fixed Building (mm)		Isolated Building (mm)	
	E_x	E_y	E_x	E_y
Ground Floor	0.00	0.00	59.52	59.17
1. Floor	4.75	4.79	69.87	69.89
2. Floor	12.23	12.46	75.01	75.46
3. Floor	19.37	19.89	78.70	79.54
4. Floor	25.31	26.13	81.47	82.66
5. Floor	29.64	30.75	83.39	84.89
6. Floor	32.19	33.59	84.53	86.30

As a result of the calculations, the required reinforcement for the 6-6 axis of the fixed and isolated building are shown in Tables 13-14.

As a result of the calculations, the required shear reinforcement for the 6-6 axis of the fixed and isolated building are shown in Tables 15-16.

The longitudinal reinforcement overlap zones and reinforcement passages were not calculated in isolated and fixed building. For the 6-6 axis, approximately 2800 kg of longitudinal reinforcement is required in the fixed structure, while approximately 1800 kg of longitudinal reinforcement is required in the isolated building. Transverse reinforcements were calculated without considering column tightening zones in isolated and fixed building. The transverse reinforcement of fixed and isolated building was calculated as approximately 670 kg and 400 kg, respectively.

4. Conclusions

In this study, the isolated building with LRB and fixed building are examined. LRB isolators used in seismic building were designed according to UBC-97. The floor displacements, internal forces, transverse and longitudinal reinforcement of selected axis of seismic isolated and fixed building are compared.

Comparing the results of this study, the following observations can be made:

- The base shear forces of isolated building are smaller than fixed building nearly about 57%. It means that the isolation system is affected to decrease lateral forces.
- The base shear forces of isolated building are smaller than fixed building about 43%.
- The maximum 6. floor displacement of building increased from 33.59 to 86.3 mm by means of using seismic isolation system. In ground floor, displacement increased from zero to 59 mm. This value is the displacement of the isolator.
- Except first floor, the diameter of required reinforcement used in a seismic isolated building is generally of smaller and greater spacing than the fixed building.
- The diameter of shear reinforcement used in a seismic isolated building is generally of smaller and greater spacing than the fixed building.
- The weight of longitudinal reinforcement of selected axis of isolated building is smaller than fixed building about 36%. It is thought that the cost of reinforcement will decrease considerably if the comparison is made in the whole building.
- The weight of transverse reinforcement of selected axis of isolated building is smaller than fixed building about 40%.

This study demonstrated that using seismically isolated building with LRB decrease required reinforcement and internal forces. So, it is thought that the using LRB decrease cost of reinforcement.

Table 13. Required reinforcement of fixed building.

	A axis	B axis	C axis	D axis
1. Floor	16ϕ25	12ϕ18	12ϕ18	16ϕ25
2. Floor	12ϕ22	12ϕ20	12ϕ20	12ϕ22
3. Floor	12ϕ22	12ϕ22	12ϕ22	12ϕ22
4. Floor	12ϕ20	12ϕ22+8 ϕ14	12ϕ22+8 ϕ14	12ϕ20
5. Floor	12ϕ18	12ϕ22+8 ϕ18	12ϕ22+8 ϕ18	12ϕ18
6. Floor	12ϕ18	12ϕ25+8 ϕ20	12ϕ25+8 ϕ20	12ϕ18

Table 14. Required reinforcement of isolated building.

	A axis	B axis	C axis	D axis
1. Floor	16ϕ22	4ϕ25+12ϕ22	4ϕ25+12ϕ22	16ϕ22
2. Floor	8ϕ20	4ϕ25+12ϕ22	4ϕ25+12ϕ22	8ϕ20
3. Floor	8ϕ20	8ϕ20	8ϕ20	8ϕ20
4. Floor	8ϕ20	8ϕ20	8ϕ20	8ϕ20
5. Floor	8ϕ20	8ϕ20	8ϕ20	8ϕ20
6. Floor	8ϕ20	8ϕ20	8ϕ20	8ϕ20

Table 15. Required shear reinforcement of fixed building.

	A axis	B axis	C axis	D axis
1. Floor	3ϕ8 / 180	4ϕ8 / 150	4ϕ8 / 150	3ϕ8 / 180
2. Floor	3ϕ8 / 180	4ϕ8 / 140	4ϕ8 / 140	3ϕ8 / 180
3. Floor	3ϕ8 / 200	4ϕ8 / 150	4ϕ8 / 150	3ϕ8 / 200
4. Floor	2ϕ8 / 190	4ϕ8 / 190	4ϕ8 / 190	2ϕ8 / 190
5. Floor	2ϕ8 / 190	2ϕ8 / 190	2ϕ8 / 190	2ϕ8 / 190
6. Floor	2ϕ8 / 190	2ϕ8 / 190	2ϕ8 / 190	2ϕ8 / 190

Table 16. Required shear reinforcement of isolated building.

	A axis	B axis	C axis	D axis
1. Floor	2ϕ8 / 200	4ϕ8 / 160	4ϕ8 / 160	2ϕ8 / 200
2. Floor	2ϕ8 / 200	2ϕ8 / 200	2ϕ8 / 200	2ϕ8 / 200
3. Floor	2ϕ8 / 200	2ϕ8 / 200	2ϕ8 / 200	2ϕ8 / 200
4. Floor	2ϕ8 / 200	2ϕ8 / 200	2ϕ8 / 200	2ϕ8 / 200
5. Floor	2ϕ8 / 200	2ϕ8 / 200	2ϕ8 / 200	2ϕ8 / 200
6. Floor	2ϕ8 / 200	2ϕ8 / 200	2ϕ8 / 200	2ϕ8 / 200

Publication Note

This research has previously been presented at the 3rd International Conference on Advanced Engineering Technologies (ICADET'19) held in Bayburt, Turkey, on September 19-21, 2019. Extended version of the research has been submitted to Challenge Journal of Structural Mechanics and has been peer-reviewed prior to the publication.

References

Abadi MMT, Adhami B (2016). Improving the seismic behavior of symmetrical steel structures under near-field earthquake using a base isolation method lead rubber bearing isolator. *Modern Applied Science*, 10(7), 10-21.

Atmaca B, Ateş Ş (2017). Determination of bearing type effect on elastomeric bearing selection with SREI-CAD. *Advances in Computational Design*, 2(1), 43-56.

Billah AM, Todorov B (2019). Effects of subfreezing temperature on the seismic response of lead rubber bearing isolated bridge. *Soil Dynamics and Earthquake Engineering*, 126, 105814.

Habieb AB, Valente M, Milani G (2019). Base seismic isolation of a historical masonry church using fiber reinforced elastomeric isolators. *Soil Dynamics and Earthquake Engineering*, 120, 127-145.

Kumar P, Petwala S (2019). Seismic performance of secondary systems housed in isolated and non-isolated building. *Earthquake and Structures*, 16(4), 401-413.

Nakhostin H, Poursha FM (2017). Applicability of the N2, extended N2 and modal pushover analysis methods for the seismic evaluation of base-isolated building frames with lead rubber bearings (LRBs). *Soil Dynamics and Earthquake Engineering*, 98, 84-100.

Reddy MR, Srujana N, Lingeshwaran N (2017). Effect of base isolation in multistoried reinforced concrete building. *International Journal of Civil Engineering and Technology*, 8(3), 878-887.

Shoaei P, Mahsuli M (2019). Reliability-based design of steel moment frame structures isolated by lead-rubber bearing systems. *Structures*, 20, 765-778.

Su L, Ahmadi G, Tadjbakhsh IG (1989). Comparative Study of base isolation systems. *Journal of Engineering Mechanics*, 115(9), 1976-1992.

Tanwer MT, Kazi TA, Desai M (2018). A study on different types of base isolation system over fixed based, *Smart Innovation, Systems and Technologies*, 106, 725-734.

Tavakoli HR, Naghavia F, Goltabar AR (2015). Effect of base isolation systems on increasing the resistance of structures subjected to progressive collapse. *Earthquakes and Structures*, 9(3), 639-656.

UBC-97 (1997). Uniform Building Code. American Structural Engineering Design Provisions, USA.

Wu Y, Wang H, Ben S, Rui-jun Z, Lin A (2018). The compression-shear properties of small-size seismic isolation rubber bearings for bridges. *Structural Monitoring and Maintenance*, 5(1), 39-50.

Zhi-hua L, Zhi-j iang H, Lei W (2016). Experimental study of seismic isolation performance of PC continuous beam bridge using lead-rubber bearings. *Bridge Construction*, 46(5), 18-23.

Challenge Journal of Structural Mechanics

Research Article

Use of trigonometric series functions in free vibration analysis of laminated composite beams

Muhittin Turan [a,*], Volkan Kahya [b]

[a] *Department of Civil Engineering, Bayburt University, 69000 Bayburt, Turkey*
[b] *Department of Civil Engineering, Karadeniz Technical University, 61080 Trabzon, Turkey*

ABSTRACT

In this study, free vibration analysis of layered composite beams is performed by using an analytical method based on trigonometric series. Based on the first-order shear deformation beam theory, the governing equations are derived from the Lagrange's equations. Appropriate trigonometric series functions are selected to satisfy the end conditions of the beam. Navier-type solution is used to obtain natural frequencies. Natural frequencies are calculated for different end conditions and lamina stacking. It was seen that the slenderness, E_{11}/E_{22} and fiber angle have a significant effect on natural frequency. The results of the study are quite compatible with the literature.

ARTICLE INFO

Article history:
Received 8 November 2019
Revised 25 December 2019
Accepted 11 January 2020

Keywords:
Laminated composite beam
Free vibration
Trigonometric functions
First-order shear deformation theory

1. Introduction

Laminated composites, which have become one of the important subjects of today, are light and corrosion resistant and have high strength. Commonly used laminated composites are used in beams, columns and plates that are structural elements, thus, it is quite essential to know and understand static and dynamic behavior of such structures.

There is an extensive research in the literature on the laminated composite beams. In these works, different analytical and numerical techniques were used. Reddy (1997) gave analytical and numerical solution procedures for bending, buckling and free vibration problems of laminated composite plates and beams considering the different lamination theories. In laminated beams, effect of shear deformation is highly important. The first-order shear deformation theory (FSDT) was thus developed to include the effect of shear. In this theory, a constant transverse shear strain through-the-thickness was assumed, and a shear correction factor must be used. However, FSDT is widely used in the analysis of laminated composite beams (Yuan and Miller, 1989; Teboub and Hajela, 1995; Banerjee, 1998; Chakraborty et al., 2002; Goyal and Kapania, 2007; Jafari-Talookolaei et al., 2012; Kahya, 2012).

The number of studies using higher-order theory is quite high in the literature. Song and Waas (1997) used the simple higher-order theory that assumes the cubic variation for the displacement field through the thickness in buckling and free vibration analyses of stepped laminated composite beams. Kant et al. (1998) presented analytical solution to the natural frequency analysis of composite and sandwich beams based on higher order refined theory. Karama et al. (1998) proposed a new laminated composite beam model based on the discrete layer theory for bending, buckling and free vibration problems of thin and thick beams. Aydogdu (2005) studied the vibration of cross-ply laminated beams subjected to different sets of boundary conditions by Ritz method is based on a three-degree-of-freedom shear deformable beam theory. Zhen and Wanji (2008) gave analytical solutions to vibration and stability problems of laminated composite and soft-core sandwich beams according to several displacement-based theories. Li et al. (2014) presented the free vibration analyses of laminated composite beams using refined higher-order shear deformation theory. Mantari and Canales (2016) provided an analytical solution for buckling and free vibration analysis of laminated beams using a refined and generalized shear deformation theory involving thickness

* *Corresponding author*. Tel.: +90-458-211-1152 ; Fax: +90-458-211-1178 ; E-mail address: mturan@bayburt.edu.tr (M. Turan)
ISSN: 2149-8024 / DOI: https://doi.org/10.20528/cjsmec.2020.02.002

expansion. Nguyen et al. (2017) developed a new trigonometric-series solution based on a higher-order theory for analysis of composite beams with arbitrary lay-ups. Kahya and Turan (2018) presented a higher-order finite element for free vibration and buckling of laminated composite and sandwich beams. Kahya et al. (2019) presented free vibration analysis of laminated composite beams including open transverse cracks by using a shear-deformable thirteen degrees-of-freedom finite element model.

This study presents an analytical method for free vibration of laminated composite beams. Free vibration analysis of layered composite beams is performed by using an analytical method based on trigonometric series. Based on the first-order shear deformation beam theory, the governing equations are derived from the Lagrange's equations. Natural frequencies are calculated for different end conditions and lamina stacking. The results of the study are quite compatible with the literature.

2. Material and Method

Consider a laminated beam as shown in Fig. 1. The displacement field of first-order shear deformation theory is given by:

$$\begin{aligned} u(x,z,t) &= u^0(x,t) - z\,\phi^0(x,t), \\ w(x,z,t) &= w^0(x,t) \end{aligned} \tag{1}$$

where u^0, w^0 and ϕ^0 are the axial and transversal displacements, and cross-sectional rotation, respectively. t is time. The strain-displacement relations are given by

$$\varepsilon_{xx} = u^0_{,x} - z\phi^0_{,x}, \qquad \gamma_{xz} = w^0_{,x} - \phi^0 \tag{2}$$

where ε_{xx} and γ_{xz} are the normal and shear strains, respectively. $(\cdot)_{,x}$ denotes the derivative with respect to x. The constitutive relations for an orthotropic ply configuration are given by

$$\sigma_{xx} = \bar{C}_{11}\varepsilon_{xx}, \quad \tau_{xz} = K\bar{C}_{55}\gamma_{xz} \tag{3}$$

where σ_{xx} and τ_{xz} are the normal and shear stresses, respectively. K is shear correction factor which is taken as 5/6 for a rectangular cross-section. $\bar{C}_{11}$ and $\bar{C}_{55}$ are the transformed material constants which are given by

$$\begin{aligned} \bar{C}_{11} &= C_{11}\cos^4\theta + 2(C_{12}+2C_{66})\cos^2\theta\sin^2\theta + C_{22}\sin^4\theta, \\ \bar{C}_{55} &= C_{55}\cos^2\theta + C_{44}\sin^2\theta \end{aligned} \tag{4}$$

where θ is the fiber angle measured from the positive x-axis in counter clockwise direction. C_{ij} terms are

$$\begin{aligned} &C_{11} = \frac{E_{11}}{1-\nu_{12}\nu_{21}}, \quad C_{12} = \frac{\nu_{12}E_{22}}{1-\nu_{12}\nu_{21}}, \quad C_{22} = \frac{E_{22}}{1-\nu_{12}\nu_{21}}, \\ &C_{44} = G_{23}, \quad C_{55} = G_{13}, \quad C_{66} = G_{12} \end{aligned} \tag{5}$$

where E_{ij} and G_{ij} denote Young's and shear modulus, respectively, ν_{ij} is Poisson's ratio.

The governing equations of motion can be obtained by Lagrange's equations which is given by

$$\frac{d}{dt}\left(\frac{\partial \prod}{\partial \dot{q}_i}\right) - \frac{\partial \prod}{\partial q_i} = 0 \tag{6}$$

where $\prod = T - (U+V)$ is the Langragian functional, q_i denotes the generalized coordinates corresponding to nodal displacements. The strain and kinetic energy of the beam can be given by

$$\begin{aligned} U &= \frac{1}{2}\int_0^L\int_A(\sigma_{xx}\varepsilon_{xx} + \tau_{xz}\gamma_{xz})dAdx = \frac{1}{2}\int_0^L\Big\{A_0\left(u^0_{,x}\right)^2 - 2A_1u^0_{,x}\phi^0_{,x} \\ &+ A_2\left(\phi^0_{,x}\right)^2 + B_0\left(\left(\phi^0\right)^2 - 2\phi^0w^0_{,x} + \left(w^0_{,x}\right)^2\right)\Big\}dx \\ T &= \frac{1}{2}\int_0^L\int_A\rho(z)(\dot{u}^2+\dot{w}^2)dAdx = \frac{1}{2}\int_0^L\Big\{I_0\left(\dot{u}^0\right)^2 \\ &- 2I_1\dot{u}^0\dot{\phi}^0 + I_2\left(\dot{\phi}^0\right)^2 + I_0\left(\dot{w}^0\right)^2\Big\}dx \end{aligned} \tag{7}$$

where

$$\begin{aligned} A_n &= \sum_{k=1}^{N}\int_{z_k}^{z_{k+1}} b\bar{C}_{11}^{(k)}z^n dx \quad (n=0,1,2), \\ B_0 &= \sum_{k=1}^{N}\int_{z_k}^{z_{k+1}} bK\bar{C}_{55}^{(k)}dx, \\ I_n &= \sum_{k=1}^{N}\int_{z_k}^{z_{k+1}} b\rho^{(k)}z^n dx \quad (n=0,1,2) \end{aligned} \tag{8}$$

where k is the layer number.

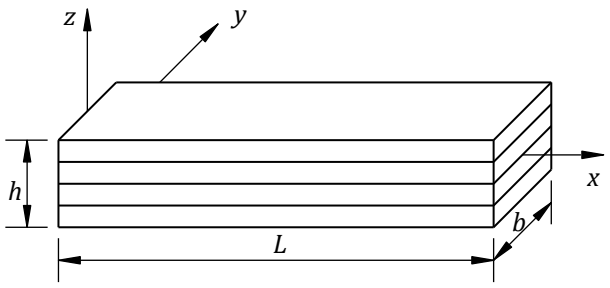

Fig. 1. Geometry and dimensions of the laminated composite beam and the co-ordinate system.

The work done by axial compressive force P_0 acting on the beam at its ends can be given by

$$V = \frac{1}{2}\int_0^L P_0\left(w^0_{,x}\right)^2 dx \tag{9}$$

Assume the solutions to $u^0(x,t)$, $w^0(x,t)$,and $\phi^0(x,t)$ as:

$$\begin{aligned} u^0(x,t) &= \sum_{i=1}^{m}\varphi_i(x)u_i(t), \\ w^0(x,t) &= \sum_{i=1}^{m}\psi_i(x)w_i(t), \\ \phi^0(x,t) &= \sum_{i=1}^{m}\theta_i(x)\phi_i(t) \end{aligned} \tag{10}$$

where $u_i(t)$, $w_i(t)$ and $\phi_i(t)$ are the generalized nodal displacements, and $\varphi_i(x)$, $\psi_i(x)$ and $\theta_i(x)$ are trigonometric functions varying depending on the end conditions of the beams, and m is the number of trigonometric series. In Table 1, trigonometric functions selected to provide support conditions for the beams considered in the study are given. Simply-supported (S-S), clamped-clamped (C-C) and clamped-free (C-F) end conditions are considered for different laminated composite beams.

If the work and energy expressions are written in the Lagrange equation, taking into account the trigonometric functions given in Table 1, the equation of motion for the L length beam is given by

$$\mathbf{M}\ddot{\mathbf{X}} + (\mathbf{K}_e - P_0\mathbf{K}_g)\mathbf{X} = \mathbf{F} \tag{11}$$

where **M**, $\mathbf{K_e}$, $\mathbf{K_g}$ and **F** are the global mass, stiffness, geometric stiffness matrices and load vector, respectively.

$$\mathbf{M} = \begin{bmatrix} \mathbf{M}_{11} & \mathbf{M}_{12} & \mathbf{M}_{13} \\ \mathbf{M}_{12}^{\mathrm{T}} & \mathbf{M}_{22} & \mathbf{M}_{23} \\ \mathbf{M}_{13}^{\mathrm{T}} & \mathbf{M}_{23}^{\mathrm{T}} & \mathbf{M}_{33} \end{bmatrix},$$

$$\mathbf{K}_e = \begin{bmatrix} \mathbf{K}_{11} & \mathbf{K}_{12} & \mathbf{K}_{13} \\ \mathbf{K}_{12}^{\mathrm{T}} & \mathbf{K}_{22} & \mathbf{K}_{23} \\ \mathbf{K}_{13}^{\mathrm{T}} & \mathbf{K}_{23}^{\mathrm{T}} & \mathbf{K}_{33} \end{bmatrix}, \tag{12}$$

$$\mathbf{K}_g = \begin{bmatrix} \mathbf{0} & \mathbf{0} & \mathbf{0} \\ \mathbf{0} & \mathbf{G}_{22} & \mathbf{0} \\ \mathbf{0} & \mathbf{0} & \mathbf{0} \end{bmatrix}, \ \mathbf{F} = \begin{Bmatrix} \mathbf{0} \\ \mathbf{F}_2 \\ \mathbf{0} \end{Bmatrix}$$

where Eq. (12) for each term is clearly defined in the Appendix. For free vibration of the beam without axial loading, ignoring $\mathbf{K_g}$ matrix and assuming $\mathbf{X} = \mathbf{u}e^{i\omega t}$ and **F**=0 in Eq. (11), we have the following eigenvalue problem:

$$(\mathbf{K}_e - \omega^2\mathbf{M})\mathbf{u} = \mathbf{0} \tag{13}$$

where ω denotes the natural frequencies of the beam. The natural frequencies of the beam can be obtained by non-trivial solutions of Eq. (13).

3. Results

In this section, numerical results of free vibration analysis of laminated composite beams with various boundary conditions are presented. Analytical results were obtained with the help of a program written in MATLAB. Simply-supported (S-S), clamped-clamped (C-C) and clamped-free (C-F) end conditions are considered for different laminated composite beams. Laminates are supposed to have equal thicknesses and made of the same orthotropic materials whose properties are followed:

Material I (Nguyen et al., 2017):
E_{11} / E_{22}= open, $G_{12} = G_{13} = 0.6E_{22}$, $G_{23} = 0.5E_{22}$, $\nu_{12} = 0.25$
Material II (Nguyen et al., 2017):
E_{11} / E_{22}= open, $G_{12} = G_{13} = 0.5E_{22}$, $G_{23} = 0.2E_{22}$, $\nu_{12} = 0.25$
Material III (Nguyen et al., 2017):
E_{11}= 144.8GPa, E_{22} = 9.65GPa, G_{12}= G_{13} = 4.14GPa, G_{23} = 3.45GPa, ν_{12} = 0.3, ρ = 1389kg/m^3

Table 1. Trigonometric functions.

Boundary Conditions	$\varphi_i(x)$	$\psi_i(x)$	$\theta_i(x)$
S-S	$\cos\frac{i\pi}{L}x$	$\sin\frac{i\pi}{L}x$	$\cos\frac{i\pi}{L}x$
C-F	$\sin\frac{(2i-1)\pi}{2L}x$	$1-\cos\frac{(2i-1)\pi}{2L}x$	$\sin\frac{(2i-1)\pi}{2L}x$
C-C	$\sin\frac{2i\pi}{L}x$	$\sin^2\frac{i\pi}{L}x$	$\sin\frac{2i\pi}{L}x$

For convenience, the following normalized terms are used:

$$\text{For Materials I and II} \ \rightarrow \ \bar{\omega} = \frac{\omega L^2}{h}\sqrt{\frac{\rho}{E_{22}}}, \qquad \text{For Materials III} \ \rightarrow \ \bar{\omega} = \frac{\omega L^2}{h}\sqrt{\frac{\rho}{E_{11}}} \tag{14}$$

In Table 2, the number of terms to be used in the analytical solution was investigated. As can be seen, sufficient accuracy is obtained with 10 terms.

The normalized fundamental frequencies are presented for cross-ply laminated beams in Table 3. The results of higher-order shear deformation theory given by Mantari and Canales (2016) and Nguyen et al. (2017) are assumed. As seen, the results are in good agreement. As the slenderness (L/h) increases, the frequencies increase, too. Here, we again observed that the agreement between the results is good for symmetrical lay-ups. However, the difference between the results becomes greater for thicker beams with unsymmetrical lay-ups.

Table 4 shows the normalized fundamental frequency for symmetric ($0/\theta/0$) and unsymmetric ($0/\pm\theta/0$) composite beams with various boundary conditions. As the fiber angle (θ) increases, the normalized natural frequencies decrease. The analytical results are consistent with the literature.

Table 2. Normalized fundamental frequencies of laminated composite beams with various boundary conditions according to the number of terms to be used in analytical solution.

Beams	m	Boundary Conditions		
		S-S	C-C	C-F
Material III (0/90/90/0) L/h = 15	2	2.5023	4.7584	0.9304
	4	2.5023	4.6798	0.9269
	6	2.5023	4.6524	0.9259
	8	2.5023	4.6384	0.9255
	10	2.5023	4.6298	0.9252
	12	2.5023	4.6240	0.9252
	16	2.5023	4.6167	0.9252
Material I (0/90) L/h = 10 E_{11}/E_{22} = 40	2	6.883	13.483	2.545
	4	6.883	13.286	2.536
	6	6.883	13.219	2.534
	8	6.883	13.185	2.533
	10	6.883	13.164	2.532
	12	6.883	13.150	2.532
	16	6.883	13.132	2.532

Table 3. Normalized fundamental frequencies of (0/90/0) and (0/90) composite beams (Material I, E_{11}/E_{22}= 40).

B.C.	Beams	Theory	L/h				
			5	10	20	30	50
S-S	(0/90/0)	Present	9.205	13.661	16.355	17.056	17.452
		Nguyen et al. (2017)	9.208	13.614	16.338	17.055	17.462
		Mantari and Canales (2016)	9.208	13.610	-	-	-
	(0/90)	Present	5.953	6.883	7.201	7.265	7.300
		Nguyen et al. (2017)	6.128	6.945	7.219	7.274	7.302
		Mantari and Canales (2016)	6.109	6.913	-	-	-
C-F	(0/90/0)	Present	4.182	5.499	6.070	6.196	6.263
		Nguyen et al. (2017)	4.234	5.498	6.070	6.198	6.267
		Mantari and Canales (2016)	4.221	5.490	-	-	-
	(0/90)	Present	2.342	2.532	2.588	2.599	2.604
		Nguyen et al. (2017)	2.383	2.543	2.591	2.600	2.605
		Mantari and Canales (2016)	2.375	2.532	-	-	-
C-C	(0/90/0)	Present	10.621	19.328	29.709	34.332	37.708
		Nguyen et al. (2017)	11.607	19.728	29.695	34.268	37.679
		Mantari and Canales (2016)	11.486	19.652	-	-	-
	(0/90)	Present	9.069	13.164	15.489	16.073	16.399
		Nguyen et al. (2017)	10.027	13.670	15.661	16.154	16.429
		Mantari and Canales (2016)	9.974	13.628	-	-	-

Table 4. Normalized fundamental frequency for symmetric and unsymmetric composite beams with various boundary conditions (Material I, E_{11} / E_{22} = 40).

L / h	Beams	S-S		C-F	
		Present	Mantari and Canales (2016)	Present	Mantari and Canales (2016)
5	(0/30/0)	9.3770	9.4651	4.2540	4.3218
	(0/45/0)	9.3142	9.3801	4.2264	4.2855
	(0/60/0)	9.2570	9.2946	4.2029	4.2519
	(0/30/-30/0)	9.3029	9.4194	4.2096	4.2821
	(0/45/-45/0)	9.1779	9.2928	4.1464	4.2129
	(0/60/-60/0)	9.0727	9.1699	4.0977	4.1548
	(0/90/0/90)	7.8579	7.7822	3.3337	3.3187
10	(0/30/0)	13.8742	13.8823	5.5764	5.5791
	(0/45/0)	13.7875	13.7795	5.5427	5.5412
	(0/60/0)	13.7190	13.6889	5.5184	5.5116
	(0/30/-30/0)	13.6945	13.7306	5.4905	5.4982
	(0/45/-45/0)	13.4676	13.5092	5.3913	5.3987
	(0/60/-60/0)	13.3053	13.3371	5.3248	5.3289
	(0/90/0/90)	10.2652	10.2007	3.9182	3.9002

Fig. 2 shows variation of the normalized fundamental frequencies with the slenderness for $(0/90)_s$ beam with properties of Material II and different end conditions. When the slenderness increases, the normalized fundamental frequencies increase, too. Effect of the slenderness is more pronounced on the results for C-C end conditions. For thicker beams (L / h < 10), we can say that the slenderness is more effective on the results.

Fig. 3 shows the effect of material anisotropy (E_{11}/E_{22}) on the normalized fundamental frequencies for $(0/90)_s$ and (0/90) composite beams with simple ends. As seen, normalized fundamental frequencies increase with increasing E_{11}/E_{22}. Any change in E_{11}/E_{22} is more effective on the results for $(0/90)_s$ beam compared to (0/90) beam. We can also see here, $(0/90)_s$ beam has greater normalized fundamental frequencies than those of (0/90) beam.

Figs. 4-6 show variation of the normalized fundamental frequencies according to fiber angles of beams with different boundary conditions having different layer arrangement are given. As the fiber angle (θ) increases, the normalized natural frequencies decrease. The values obtained for (0 / θ) are greater than those obtained for (θ) and (θ / -θ)$_s$. The results are the same for (θ) and (θ / -θ)$_s$

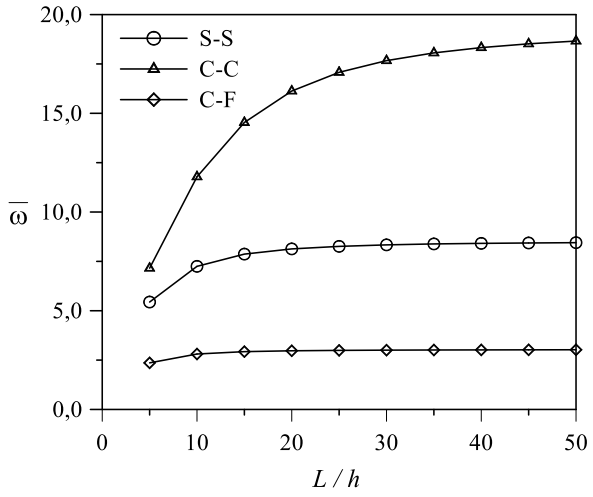

Fig. 2. Variation of the normalized fundamental frequency with span-to-depth ratio for $(0/90)_s$ laminated beam (Material II, E_{11}/E_{22} = 10).

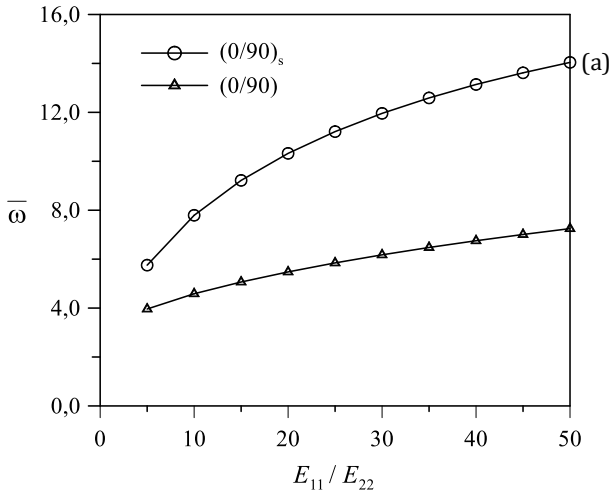

Fig. 3. Variation of the normalized fundamental frequency with E_{11}/E_{22} for (0/90) and $(0/90)_s$ simple beams (Material I, L/h=10).

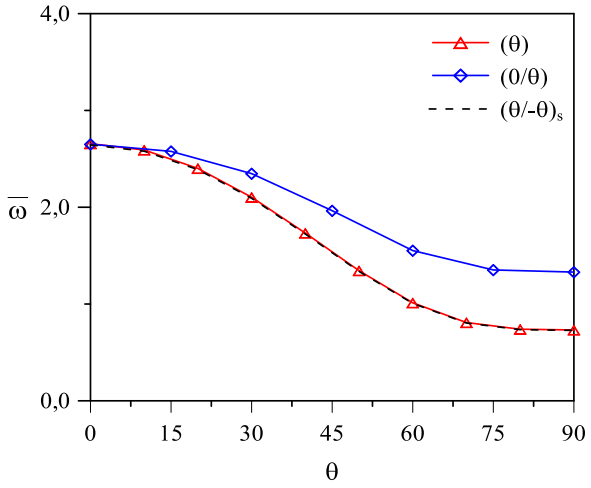

Fig. 4. Variation of the normalized fundamental frequency of simple beams according to fiber angle (θ) (Material III, L / h = 15).

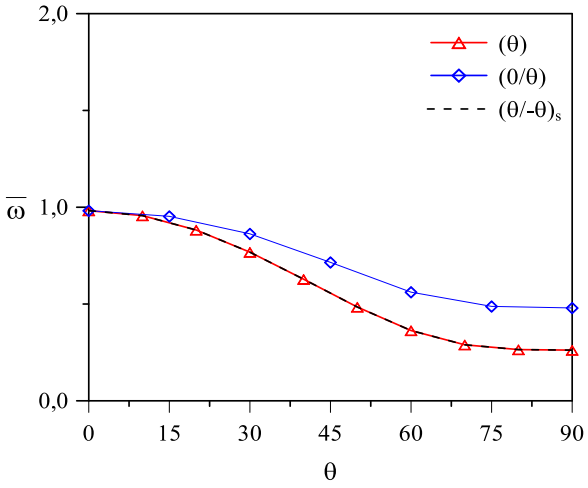

Fig. 5. Variation of the normalized fundamental frequency of cantilever beams according to fiber angle (θ) (Material III, L / h = 15).

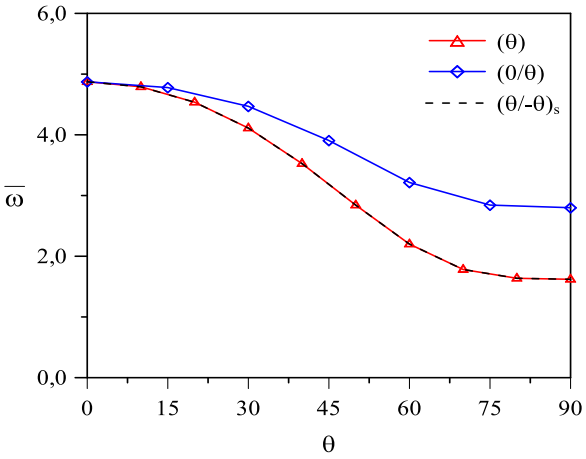

Fig. 6. Variation of the normalized fundamental frequency of fixed-ended beams according to fiber angle (θ) (Material III, L / h = 15).

4. Conclusions

Free vibration analysis of layered composite beams is performed by using an analytical method based on trigonometric series. Based on the first-order shear deformation beam theory, the governing equations are derived from the Lagrange's equations. Appropriate trigonometric series functions are selected to satisfy the end conditions of the beam. Navier-type solution is used to obtain natural frequencies. Natural frequencies are calculated for different end conditions and lamina stacking. The results of the study are quite compatible with the literature. According to results of the study:

- The slenderness (L/h) increases, the normalized fundamental frequencies increase, too.
- As the fiber angle (θ) increases, the normalized natural frequencies decrease.
- For thicker beams (L / h < 10), we can say that the slenderness is more effective on the results.
- As seen, normalized fundamental frequencies increase with increasing E_{11}/E_{22}.

Appendix A. *Elements of the global mass matrices*

$$\mathbf{M}_{11} = \mathbf{M}_{22} = \begin{bmatrix} \frac{L}{2} I_0 & 0 & 0 \\ 0 & \ddots & 0 \\ 0 & 0 & \frac{L}{2} I_0 \end{bmatrix}_{mxm}$$

$$\mathbf{M}_{12} = \mathbf{M}_{12}^{\mathrm{T}} = \mathbf{M}_{23} = \mathbf{M}_{23}^{\mathrm{T}} = 0$$

$$\mathbf{M}_{13} = \mathbf{M}_{13}^{\mathrm{T}} = \begin{bmatrix} \frac{L}{2} I_1 & 0 & 0 \\ 0 & \ddots & 0 \\ 0 & 0 & \frac{L}{2} I_1 \end{bmatrix}_{mxm}$$

$$\mathbf{M}_{33} = \begin{bmatrix} \frac{L}{2} I_2 & 0 & 0 \\ 0 & \ddots & 0 \\ 0 & 0 & \frac{L}{2} I_2 \end{bmatrix}_{mxm} \quad \text{(A1)}$$

Appendix B. *Elements of the global stiffness matrices*

$$\mathbf{K}_{11} = \begin{bmatrix} \frac{1^2\pi^2}{2L}A_0 & 0 & 0 \\ 0 & \ddots & 0 \\ 0 & 0 & \frac{m^2\pi^2}{2L}A_0 \end{bmatrix}_{mxm}$$

$$\mathbf{K}_{12} = \mathbf{K}_{12}^{\mathrm{T}} = 0$$

$$\mathbf{K}_{13} = \begin{bmatrix} \frac{1^2\pi^2}{2L}A_1 & 0 & 0 \\ 0 & \ddots & 0 \\ 0 & 0 & \frac{m^2\pi^2}{2L}A_1 \end{bmatrix}_{mxm}$$

$$\mathbf{K}_{23} = \mathbf{K}_{23}^{\mathrm{T}} = \begin{bmatrix} \frac{1\pi}{2}B_0 & 0 & 0 \\ 0 & \ddots & 0 \\ 0 & 0 & \frac{m\pi}{2}B_0 \end{bmatrix}_{mxm}$$

$$\mathbf{K}_{22} = \begin{bmatrix} \frac{1^2\pi^2}{2L}B_0 & 0 & 0 \\ 0 & \ddots & 0 \\ 0 & 0 & \frac{m^2\pi^2}{2L}B_0 \end{bmatrix}_{mxm}$$

$$\mathbf{K}_{33} = \begin{bmatrix} \frac{L}{2}B_0 + \frac{1^2\pi^2}{2L}A_2 & 0 & 0 \\ 0 & \ddots & 0 \\ 0 & 0 & \frac{L}{2}B_0 + \frac{m^2\pi^2}{2L}A_2 \end{bmatrix}_{mxm} \quad \text{(A2)}$$

Appendix C. *Elements of the geometric stiffness matrices*

$$\mathbf{G}_{22} = \begin{bmatrix} \frac{1^2\pi^2}{2L} & 0 & 0 \\ 0 & \ddots & 0 \\ 0 & 0 & \frac{m^2\pi^2}{2L} \end{bmatrix}_{mxm} \quad \text{(A3)}$$

Appendix D. *Load vector*

$$\mathbf{F}_2 = \begin{bmatrix} \frac{Lq}{1\pi} - \frac{Lq\cos(1\pi)}{1\pi} \\ \vdots \\ \frac{Lq}{m\pi} - \frac{Lq\cos(m\pi)}{m\pi} \end{bmatrix}_{mx1} \quad \text{(A3)}$$

Publication Note

This research has previously been presented at the 3rd International Conference on Advanced Engineering Technologies (ICADET'19) held in Bayburt, Turkey, on September 19-21, 2019. Extended version of the research has been submitted to Challenge Journal of Structural Mechanics and has been peer-reviewed prior to the publication.

References

Aydogdu M (2005). Vibration analysis of cross-ply laminated beams with general boundary conditions by Ritz method. *International Journal of Mechanical Sciences*, 47, 1740–1755.

Banerjee JR (1998). Free vibration of axially loaded composite Timoshenko beams using the dynamic stiffness matrix method. *Computers & Structures*, 39, 197-208.

Chakraborty A, Mahapatra RD, Gopalakrishan S (2002). Finite element analysis of free vibration and wave propagation in asymmetric composite beams with structural discontinuities. *Composite Structures*, 55, 23-36.

Goyal VK, Kapania RK (2007). A shear-deformable beam element for the analysis of laminated composites. *Finite Elements in Analysis and Design*, 43, 463-477.

Jafari-Talookolaei RA, Abedi M, Kargarnovin MH, Ahmadian MT (2012). An analytical approach for the free vibration analysis of generally laminated composite beams with shear effect and rotary inertia. *International Journal of Mechanical Sciences*, 65, 97–104.

Kahya V (2012). Dynamic analysis of laminated composite beams under moving loads using finite element method. *Nuclear Engineering and Design*, 243, 41-48.

Kahya V, Turan M (2018). Vibration and buckling of laminated beams by a multi-layer finite element model. *Steel and Composite Structures*, 28, 415-426.

Kahya V, Sebahat K, Okur FY, Altunışık AC, Aslan M (2019). Free vibrations of laminated composite beams with multiple edge cracks: Numerical model and experimental validation. *International Journal of Mechanical Sciences*, 159, 30-42.

Kant T, Marur SR, Rao GS (1998). Analytical solution to the dynamic analysis of laminated beams using higher order refined theory. *Composite Structures*, 40, 1–9.

Karama M, Abou Harb B, Mistou S, Caperaa S (1998). Bending, buckling and free vibration of laminated composite with a transverse shear stress continuity model. *Composites Part B: Engineering*, 29(3), 223-234.

Li J, Huo Q, Li X, Kong X, Wu W (2014). Vibration analyses of laminated composite beams using refined higher-order shear deformation theory. *International Journal of Mechanics and Materials in Design*, 10, 43-52.

Mantari JL, Canales FG (2016). Free vibration and buckling of laminated beams via hybrid Ritz solution for various penalized boundary conditions. *Composite Structures*, 152, 306–315.

Nguyen TK, Nguyen ND, Vo TP, Thai HT (2017). Trigonometric-series solution for analysis of laminated composite beams. *Composite Structures*, 160, 142-151.

Reddy JN (1997). Mechanics of Laminated Composite Plates: Theory and Analysis. CRC Press, Boca Raton.

Song SJ, Waas AM (1997). Effects of shear deformation on buckling and free vibration of laminated composite beams. *Composite Structures*, 37(1), 33-43.

Teboub Y, Hajela P (1995). Free vibration of generally layered composite beams using symbolic computations. *Composite Structures*, 33, 123-134.

Yuan FG, Miller RE (1989). A new finite element for laminated composite beams. *Computers & Structures*, 31, 737-45.

Zhen W, Wanji C (2008). An assessment of several displacement theories for the vibration and stability analysis of laminated composite and sandwich beams. *Composite Structures*, 84, 337-349.

Challenge Journal of Structural Mechanics

Research Article

Comparison of short- and long-term ASR test methods on cementitious composites

Burak Sivrikaya [a], İlhami Demir [b,*], Özer Sevim [b]

[a] *Department of Building Inspection, Kaman Vocational School, Kırşehir Ahi Evran University, 40300 Kırşehir, Turkey*
[b] *Department of Civil Engineering, Kırıkkale University, 71450 Kırıkkale, Turkey*

ABSTRACT

Concrete has a significant place in construction structures, is a material that can be easily damaged due to incorrect design, incorrect material selection. Concrete may be damaged by physical and chemical factors. One of these factors is the alkali-silica reaction (ASR). ASTM C1260, is a short-term test method, and ASTM C227, is a long-term test method, are used to measure effect of alkali-silica reaction. In this study, the effect of fly ash additive use with 0, 5, 10, 15, and 20 wt.% replacement of cement was investigated in short- and long-term ASR test methods. For this purpose, while samples prepared for ASTM C1260 were kept in NaOH solution 14-days, samples prepared for ASTM C227 were waited 360-days in normal water solution. As a result; mortar bars with 20% fly ash additive ratio were classified as harmless for ASR in both test methods.

ARTICLE INFO

Article history:
Received 15 November 2019
Revised 13 December 2019
Accepted 8 January 2020

Keywords:
ASTM C1260
ASTM C227
Fly ash
Alkali-silica reaction

1. Introduction

Alkali–silica reaction (ASR) is a chemical reaction that forms between aggregates having reactive silica forms and alkali oxides, resulting from expansion. As a result of the chemical reaction, alkali-silica gels are formed in the concrete. This material has high water absorption capacity. When the concrete is in a humid environment, those gels swell by absorbing water. Swollen gels cause stresses in the concrete and cause capillary cracks. This phenomenon is called "Alkali-Silica Reaction (ASR). This reaction simply occurs in two stages. In the first stage, ASR gel products are created by the combination of reactive silica gels with alkali and then, in the second stage, the created alkali-silica gels expand in the presence of moisture in the environment at a suitable temperature. The resulting expansion also causes cracking and deterioration of concrete over time (Demir and Arslan, 2013; Demir and Sevim, 2017; Demir et al., 2018).

The damage caused by ASR in concrete was first introduced as a case by Stanton in North America in 1940 and has since been known in many countries (Stanton, 1940; Fronhnsdorff, 1978). Many studies have been published since Stanton, but the ASR mechanism has not yet been fully understood (Hobbs, 1998; Diamond and Penko, 1992; Helmuth et al., 1993; Copra and Bournazel, 1995). Studies are carrying out minimizing the effect of ASR, one of these is the use of mineral additives. The use of mineral additives can improve the compressive strength, permeability and void structure of mortar and concrete over time (Bagel, 1998). Due to the hydration process associated with mineral admixtures, the total void ratio of concrete or mortar is reduced (Dongxue et al., 1997). Mineral additives such as silica fume and fly ash are also known to reduce ASR expansions (Monteiro et al., 1997; Ramlochan et al., 2000). To investigate the effects of these mineral additives, accelerated test method (ASTM C1260) is generally preferred. While samples prepared for ASTM C1260 are kept in NaOH solution for 14 days (ASTM C1260-14, 2014), samples prepared for ASTM C227 should be waited 360 days in normal water solution (ASTM C227-10, 2010).

In this study, fly ash was replaced by cement in 5, 10, 15, 20 wt.% and mortar bars were prepared for both test methods. The prepared mortar bars were exposed separately to both test methods and resulting ASR effects were compared.

* *Corresponding author*. Tel.: +90-318-357-4242 ; Fax: +90-318-357-2459 ; E-mail address: ildemir@kku.edu.tr (İ. Demir)
ISSN: 2149-8024 / DOI: https://doi.org/10.20528/cjsmec.2020.02.003

2. Experimental Program

For the test samples to be prepared in the study, cement with an amount of alkali ratio over 0.6% is required for the formation of ASR in both test methods. Cement met the specified alkali content was used in the preparation of the samples. The chemical content of the cement used in this study is given in Table 2. Aggregates with the same particle size distribution were used for each test bar. The particle size analysis of these aggregates is given in both test methods. The particle size distribution analysis for the aggregate in the experimental methods is given in Table 1.

Table 1. Particle size distribution requirements.

Sieve Size		Percent (%)
Passing	Retained	
4.75 mm (No. 4)	2.36 mm (No. 8)	10
2.36 mm (No. 8)	1.18 mm (No. 16)	25
1.18 mm (No. 16)	600 μm (No. 30)	25
600 μm (No. 30)	300 μm (No. 50)	25
300 μm (No. 50)	150 μm (No. 100)	15

The aggregates to be used for both test methods were sieved according to the particle size distribution ratios indicated in Table 1 and prepared by mixing according to the desired ratios.

ASTM C1260 and ASTM C1260 are test methods used to measure the effect of mineral and chemical additives on length expansions caused by alkali silica reaction. ASTM C1260 is a short-term test method, resulting in 16 days. ASTM C1260 is preferred in ASR studies because it gives results in a short time. In mortar bars to be prepared according to ASTM C1260, aggregates should be 2.25 times bigger than the amount of cement and water/cement ratio of 0.47 are required. The dimensions of the mortar bars to be prepared are 25×25×285 mm. Samples prepared according to ASTM C1260 are kept in 1N NaOH solution. NaOH solution required for curing is obtained by mixing 40 g NaOH to 900 g water. Mortar bars prepared in accordance with ASTM C1260 are poured into molds. Samples poured into the molds are kept in the mold for 24 hours. After 24 hours, the samples are removed from the mold. Removed samples are stored at 80°C in 1N NaOH solution for 24 hours. After this time the first measurement is done, then after keeping samples in 80°C in NaOH solution again for 7 and 14 days, other measurements are being done, too, then the test being resulted. Expansion values are calculated after the measurements. Risk assessment is performed according to the obtained expansion results. Samples with an expansion rate greater than 0.2% are considered risky for ASR. Samples with an expansion rate between 0.2% and 0.1% are considered as risky with acceptable risk and samples with an expansion rate below 0.1% are considered risk-free for ASR.

ASTM C227 test method is a test method that lasts at least 180 days. In mortar bar samples to be prepared according to ASTM C227, aggregates should be 2.25 times bigger than the amount of cement and the water/cement ratio should be 0.47. The mortar bars should be in 25×25×285 mm dimensions. Samples prepared according to ASTM C227 are being poured into molds. After the samples are being kept in the mold for 24 hours, the first readings are made. Samples prepared according to ASTM C227 should be kept on 38°C water without contact to water and in upright position. The 2, 7, 28, 90, 180-days length expansion values of the samples are measured, and the expansion rates are calculated. According to ASTM C227, cement mortar bars are evaluated with the expansion values obtained in 6-month periods for the alkali silica reaction. According to ASTM C227, samples that are above 0.1% expansion rate are considered as risky for ASR. Samples below 0.1% expansion rate are considered safe for ASR.

When the ASTM C1260 and ASTM C227 test methods are compared, it is seen that the preparation steps of the mortar bars are the same. The aggregate gradation, the required cement alkali ratio and the water/cement ratios to be used for the mixture are given the same. The two test methods have different curing conditions. Samples prepared according to ASTM C1260 are kept in 80°C in 1N NaOH solution, while samples prepared according to ASTM C227 are kept on the water surface having a temperature of 38°C for at least 180 days without contact with water.

Mortar bars were prepared with the same amount of water, cement and aggregate content according to the water/cement/aggregate ratio specified in ASTM C1260 and ASTM C227. 0%, 5%, 10%, 15%, 20% fly ash substitutes were made in the prepared mortar bars. The prepared mortar bars are in 25 × 25 × 285 mm dimensions. The mortar bars were removed from the mold after being kept at 23 ± 2°C for 24 hours. After the mortar bars were removed from the mold, they were kept in the curing environments prepared according to the test methods for the periods specified in the test standards. The chemical properties of cement and fly ash used in the preparation of mortar bars are given in Table 2.

Table 2. Chemical properties.

Chemical Composition (%)	Cement	Fly Ash
SiO_2	18.79	57.11
Al_2O_3	5.05	19.27
Fe_2O_3	2.54	9.21
CaO	63.28	5.31
MgO	2.23	2.03
K_2O	0.83	2.39
Na_2O	0.28	0.64
SO_3	3.44	0.13
$Cr2O_3$	0.03	0.02
Mn_2O_3	0.06	0.08
TiO_2	0.26	0.90
Loss on Ignition	3.20	3.24
$Na_2O+0,658\times K_2O$	0.82	-

After the samples prepared by using aggregate, cement, water and fly ash substitution rates given in Table 3, removed from the mold, the steps for the two test methods continued differently. Mortar bars subjected to ASTM C 1260 test method were kept in 80 ± 2°C normal water for 24 hours and the first length measurements were made. Samples were measured after being kept in 80 ± 2°C 1N NaOH solution for 14 days and the test being resulted after measurement.

The samples subjected to ASTM C227 test method were taken from the mold and first length measurements were being made. After measurement, samples were kept in a test apparatus which was prepared to avoid any contact with water on 38 ± 2°C normal water for 360 days. During this period, interim measurements of 7, 28, 90, 180-days were made and the final length measurements were made after 360 days, then the test was resulted.

Length expansions at the end of both test methods and length expansions during tests were calculated. ASR effect was determined with length growth ratios obtained from these test methods. ASR effect was determined as stated in related standards and comparisons were made for both experimental standards.

Table 3. Mixture amounts of cementitious composites (g).

Ingredient	Reference	5% FA	10% FA	15% FA	20% FA
Cement	440	418	396	374	352
Aggregate	990	990	990	990	990
Water	206.8	206.8	206.8	206.8	206.8
Fly Ash	0	22	44	66	88

3. Experimental Results and Discussion

As a result of the expansion values obtained from the studies, expansion rates were calculated. Expansion rates of the samples kept under curing conditions specified in ASTM C1260 are given in Fig. 1. Expansion values of the samples kept under curing conditions specified in ASTM C227 are given in Fig. 2.

When the expansion rates given in Fig. 1. of the samples kept under curing conditions according to ASTM C 1260 were examined; fly ash additive for mortar bars seems to reduce ASR effect. The fly ash additive ratio was 20% at most. When fly ash additive ratio was performed up to 20%, the ASR effect decreased with increasing substitution rate.

When the expansion rates of the samples kept under cure conditions in accordance with ASTM C227 were examined, it was observed that the additive ratio of fly ash reduced the ASR effect. In the study, fly ash replacement was made for ASTM C227 at the rate of 20%. The ASR effect was reduced as fly ash additive ratio increased up to 20%, including 20% additive ratio. When these results are compared, it is possible to say that ASTM C227 and ASTM C1260 give a similar result. The expansion values obtained as a result of the studies for both experimental methods are given in Table 4, comparatively.

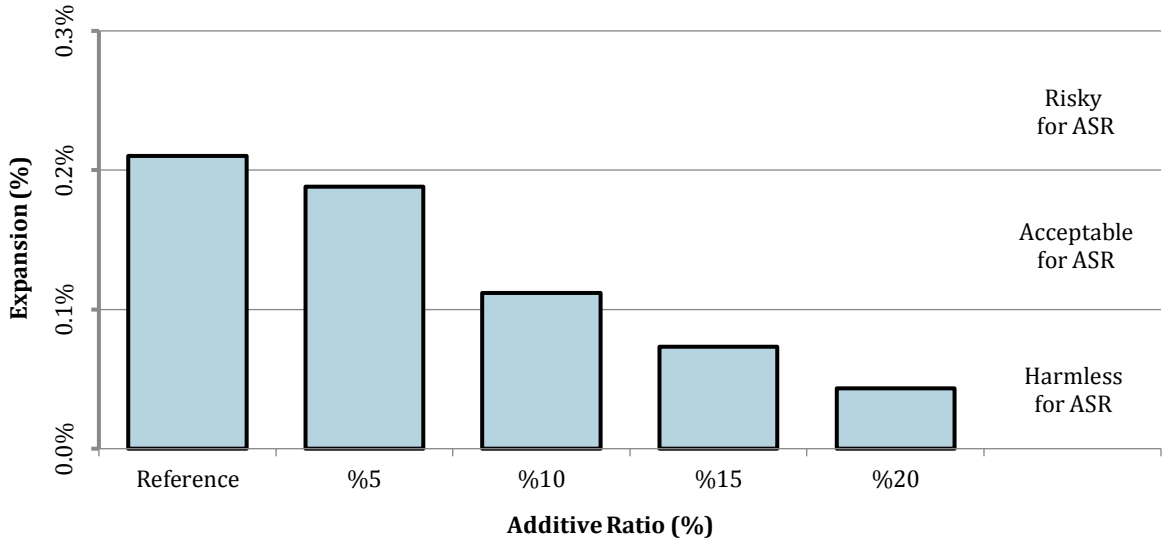

Fig. 1. Expansion ratios of the samples kept under curing conditions specified in ASTM C1260.

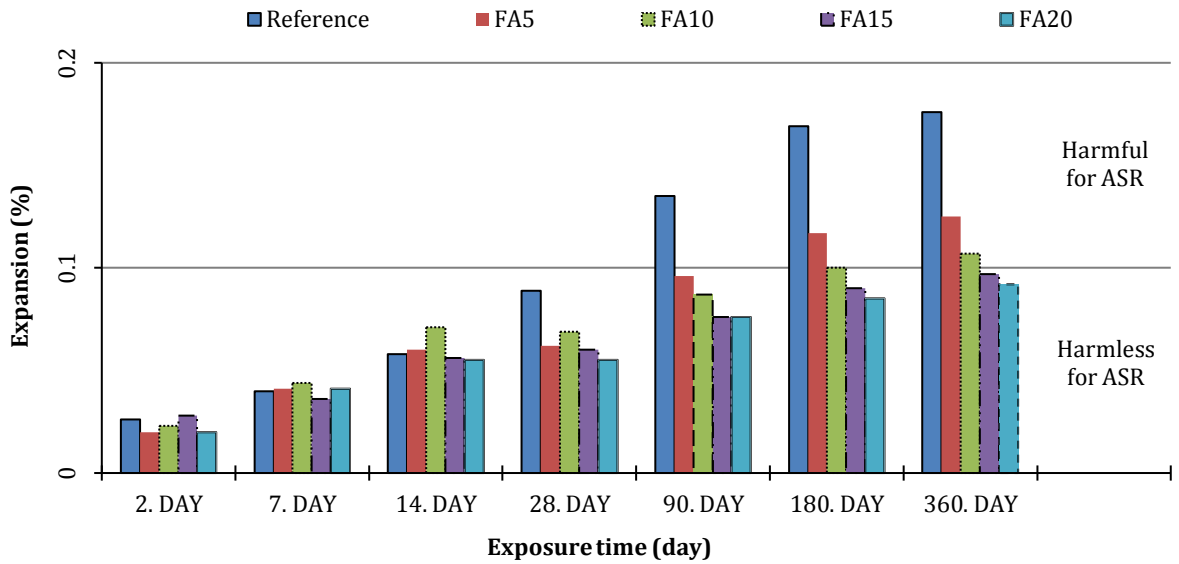

Fig. 2. Expansion values of mortar bars incorporating fly ash according to ASTM C227.

Table 4. Length expansion rates (%).

Additive Ratio	ASTM C1260 (14 day)	ASTM C227 (360 day)
0% (Reference)	0.210	0.175
5%	0.188	0.125
10%	0.112	0.107
15%	0.073	0.097
20%	0.044	0.092

When the comparative values given in the table were examined, the reference sample was considered as risky for ASR by staying above the risky ASR limit in both experimental methods.

According to the ASTM C 1260 test method, the reference sample expanded more than 0.2%, which is the limit value for harmful ASR. As a result, it was considered as harmful ASR. 5% and 10% fly ash substitute mortar bars were classified as acceptable harmful ASR according to ASTM C1260, remaining between 0.1% and 0.2%.

15% and 20% fly ash additive ratio were remained below 0.1% limit value and classified as harmless. When ASR effect was examined according to the short-term test method, it was seen that fly ash additive ratio reduces the ASR effect as well as 20% fly ash replacement reduced the ASR effect by 80% in comparison to the reference sample (Fig. 3).

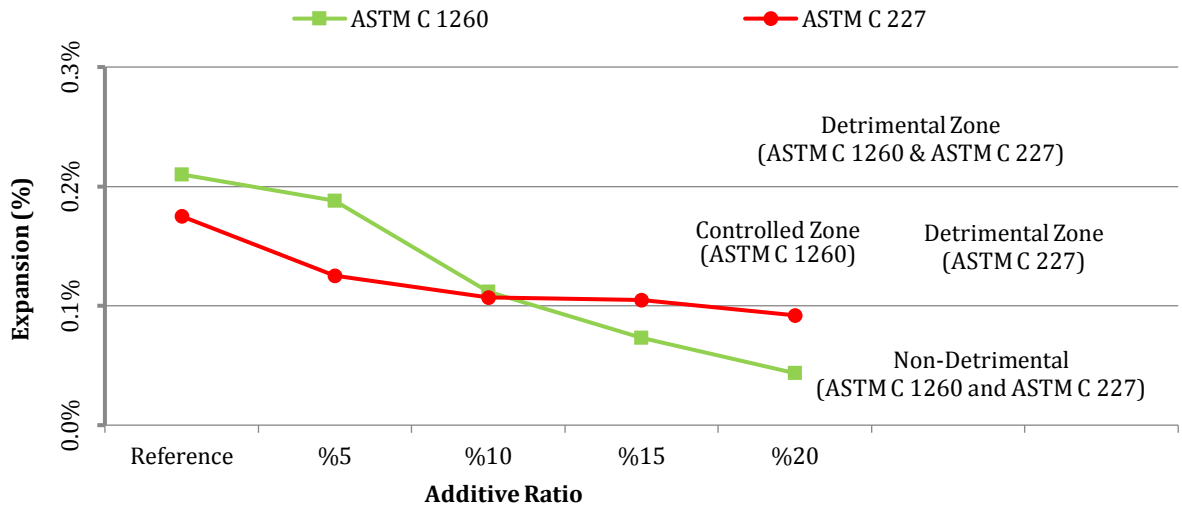

Fig. 3. Length change expansion ration of mortars bars having different fly ash replacement.

According to ASTM C227 test method, the reference sample remained in the harmful area by showing an expansion above 0.1% limit value. According to this test method, 5%, 10% and 15% fly ash replacement were evaluated as harmful ASR. Samples with 20% fly ash was below 0.1% expansion limit and classified as harmless for ASR.

When both experimental methods were compared, the reference sample was classified as harmful ASR. While mortar bars with 5% and 10% additive ratio are classified as acceptable ASR according to ASTM C1260, they are classified as harmful ASR according to ASTM C227 test method. Mortar bars with 15% fly ash additive ratio was classified as acceptable ASR according to ASTM C1260, whereas it was classified as harmless ASR according to ASTM C227 test method. Mortar bars with 20% fly ash additive ratio were classified as harmless for ASR in both test methods.

The sample preparation steps of both test methods appear to be the same. However, the difference in curing conditions constitutes the difference of the two test methods. In this study, it was seen that long-term and short-term test methods gives approximately the same result. It is understood that ASTM C1260 short-term test method does not give a healthy result in long-term experiments. It has been seen that the use of long-term test methods to learn the effect of ASR on cement in later ages will give more healthy results.

4. Conclusions

In this study, the differences between the accelerated test method ASTM C1260 and ASTM C227 test methods were compared. As a result of the study, it was observed that the samples with the same preparation phases can produce different results depending on the amount of material in the content. In studies related to ASR, chemical ASR test methods can be used to examine whether these differences are mediated by ASR or otherwise. As a result of the test methods of ASTM C1260 and ASTM C227, the expansion ratios were different in the long term.

Publication Note

This research has previously been presented at the 3rd International Conference on Advanced Engineering Technologies (ICADET'19) held in Bayburt, Turkey, on September 19-21, 2019. Extended version of the research has been submitted to Challenge Journal of Structural Mechanics and has been peer-reviewed prior to the publication.

References

ASTM C1260-14 (2014). Standard Test Method for Potential Alkali Reactivity of Aggregates (Mortar-Bar Method). ASTM International, West Conshohocken, PA.

ASTM C227-10 (2010). Standard Test Method for Potential Alkali Reactivity of Cement-Aggregate Combinations (Mortar-Bar Method). ASTM International, West Conshohocken, PA.

Bagel L (1998). Strength and pore structure of ternary blended cement mortars containing blast furnace slag and silica fume. *Cement and Concrete Research,* 28(7), 1011–1022.

Capra B, Bournazel JP (1995). Perspectives nouvelles pour la prise en compte des alcali-réactions dans le calcul des structures. *Materials and Structures*, 28(2), 71–73.

Demir İ, Arslan M (2013). The mechanical and microstructural properties of Li2SO4, LiNO3, Li2CO3 and LiBr added mortars exposed to alkali–silica reaction. *Construction and Building Materials*, 42, 64–77.

Demir İ, Sevim Ö (2017). Effect of sulfate on cement mortars containing Li2SO4, LiNO3, Li2CO3 and LiBr. *Construction and Building Materials*, 156, 46–55.

Demir İ, Sevim Ö, Kalkan İ (2018). Microstructural properties of lithium-added cement mortars subjected to alkali–silica reactions. *Sādhanā*, 43(7), 112.

Diamond S, Penko M (1992). Alkali–silica reaction processes: the conversion of cement alkalies to alkali hydroxide. *Proceedings of the Symposium on Durability of Concrete, ACI SP-131*, 131, 153–168.

Dongxue L, Xinhua F, Xuequan W, Mingshu T (1997). Durability study of steel slag cement. *Cement and Concrete Research*, 27(7), 983–987.

Frohnsdorff G, Clifton JR, Brown PW (1978). History and status of standards relating to alkalies in hydraulic cements. *ASTM International, Cement Standards-Evolution and Trends*, West Conshohocken, PA.

Helmuth R, Stark D, Diamond S, Moranville-Regourd M (1993). Alkali–Silica Reactivity: An Overview of Research. National Research Council, Washington, DC.

Hobbs DW (1988). Alkali–Silica Reaction in Concrete. Thomas Telford Publishing, Michigan.

Monteiro PJM, Wang K, Sposito G, Dos Santos MC, de Andrade WP (1997). Influence of mineral admixtures on the alkali–aggregate reaction. *Cement and Concrete Research*, 27(12), 1899–1909.

Ramlochan T, Thomas M, Gruber KA (2000). The effect of metakaolin on alkali–silica reaction in concrete. *Cement and Concrete Research*, 30(3), 339–344.

Stanton TE (1940). Influence of cement and aggregate on concrete expansion. *Engineering News-Record*, 59-61.

Challenge Journal of Structural Mechanics

Research Article

The effect of different fineness values of Afşin Elbistan fly ash on permeability in concrete

Demet Demir Şahin [a,*], Mustafa Çullu [b], Hasan Eker [c]

[a] *Department of Mining Technology, Gümüşhane University, 29000 Gümüşhane, Turkey*
[b] *Department of Civil Engineering, Gümüşhane University, 29000 Gümüşhane, Turkey*
[c] *Department of Mining Engineering, Gümüşhane University, 29000 Gümüşhane, Turkey*

ABSTRACT

Too much CO_2 is released during cement production. In many researches, the use of natural or recycled compounds plays an important role in the cement composition. The use of these components contributes both to reducing the amount of waste and to protecting the environment in nature. It is possible to produce an environmentally friendly concrete, thanks to its being a fly ash thermal power plant waste and its use as mineral additive in terms of its composition. In this study, it is aimed to produce impermeable concretes with the use of C type fly ash as substitutes for cement in concrete composition in substitution rates of 10 %, 30 % and 50 %. In order to reduce the permeability of concrete in this direction, as a result of grinding the fly ash in the ball mill for 0, 10, 20, 30, 45 and 60 minutes, concrete samples were prepared with and without admixture (Reference). Capillarity test was performed to determine the permeability at the end of cure periods of 28 and 90 days on concrete samples. According to the results obtained at the end of 28 days, the best impermeability was achieved in the mixture with 50 % fly ash replacement and 60 minutes grinding time. In 90 days, the best impermeability was obtained in the mixture with 30 % fly ash replacement and 0 minutes of grinding time. As a result, it was seen that permeability decreased with increasing thinness and substitution rate of fly ash in concrete composition.

ARTICLE INFO

Article history:
Received 15 November 2019
Revised 6 January 2020
Accepted 20 January 2020

Keywords:
Fly ash
Concrete
Cement
Permeability
C type

1. Introduction

The presence of rich lignite deposits in our country, easy to supply, short-term and low-cost operation in terms of electrical power generation is one of the most preferred reasons for thermal power plants. The increase in electricity production in the 21st century is an indicator of economic and social development and is one of the factors facilitating human life (Özcan et al., 2014). As of the end of July 2017, the number of power plants generating electricity in our country increased to 3,098 (including unlicensed plants). 613 of the existing power plants are hydroelectric, 40 are coal, 186 are wind, 33 are geothermal, 288 are natural gas, 1,773 are solar and have other sources. Afşin Elbistan thermal power plant has the highest electricity generation capacity among these power plants and the installed capacity was determined as 2795 MW in total A and B plants (MENR, 2018). In our country, the amount of fly ash released in these plants and other coal-fired thermal power plants is calculated as 18 million tons annually (Bilir et al., 2015). In the world, this amount is 780 million tons annually (Toniolo and Boccaccini, 2017).

The waste material, which is not involved in the act of burning as a result of the burning of coal in thermal power plants, which is inorganic and small in size, is transported by flue gases and collected with the help of electron filters and cyclones is termed fly ash. The formation mechanism of this product is brought to fine grain structure by the grinding of coal in ball or roller mills during electricity production. The carbon in the coal starts to ignite in the combustion chambers, which

* *Corresponding author*. Tel.: +90-456-233-2937 ; E-mail address: demetsahin@gumushane.edu.tr (D. Demir Şahin)
ISSN: 2149-8024 / DOI: https://doi.org/10.20528/cjsmec.2020.02.004

have a temperature of 1037-1482°C and are fed by continuous air. Subsequently, as a result of the continuous combustion of the coal, the volatiles evaporate and the carbon is heated in the pipes in the boiler. Inorganic materials such as clay, quartz and feldspar melt and slag is formed in the combustion chambers. Hardened melts in the flue gas are separated from the combustion chambers and spherical grained fly ash particles are formed (Hoffman, 2006).

With the increase in the need for energy and the supply of energy from coal in our country, the amount of fly ash released from thermal power plants has increased. The increase in the amount of ash led to the idea of evaluating waste in other areas. It is considered as a suitable material for use in the construction sector. However, it is more widely used in cement and concrete construction due to its composition and many other properties. Especially the fly ashes' having pozzolanic properties leads to energy saving in concrete and cement technology and to an increase in the strength and durability of concrete by the introduction of new features in fresh and hardened condition. Afşin Elbistan increases the ultimate pressure of concrete by increasing the cohesion by using fly ash with high CaO content such as fly ash. In addition, large masses such as dam structures reduce thermal shrinkage in concrete. Fly ash is collected in the chimneys and used as it can be of fine grain thickness without any treatment. Occasionally, when grain fineness is not suitable for use in concrete and cement composition, it is rendered suitable by sieving and grinding processes. In particular, the use of fly ash with fine grain structure in the composition of concrete makes a great contribution to the production of impermeable concrete (Binici et al., 2009). In addition, environmental problems and consumption of natural resources will be reduced by the use of fly ash in concrete and will contribute to the national economy with the efficient use of waste products.

Cement is an important and integral component in concrete composition. However, producing excess cement and using it in concrete composition increases the heat of hydration, shrinkage and cost. Fly ash is a waste product that form spontaneously in thermal power plants and is used instead of cement. The use of fly ash in concrete is very common and serves to reduce the heat of hydration and the microcrack structure. Thus, greenhouse gas emissions stemming from cement production are reduced. Particularly, fly ashes' having fine-grained, spherical grain structure and smooth surface characteristics, reduces the need for water in concrete and increases processability. However, the fly ashes' having pozzolanic properties also helps to regulate the gap structure (Qiu et al., 2014).

The bearing property of the concrete depends on the durability and service life of the concrete. Permeability of water is an important factor for concrete durability. As it activates the acid mechanical reaction together with chlorine, sulfate ions and water in the concrete, it accelerates the deterioration of the concrete structure. Permeability of concrete depends on the permeability of cement paste. The void structure of the concrete is the most important factor controlling the transport properties of the hydrated cement paste.

The pores of the aggregates in the concrete composition have no effect on the permeability of the concrete because the pores in the aggregate are wrapped with cement paste and permeability in concrete is affected by the porous structure of the cement paste (Neville, 1995). Permeability in cement paste is provided by capillary voids. Capillary void size is between 0.0110 m and 10 μm and voids less than this size are called gel voids. In addition to the capillary gaps, the other gap parameters, gap size and the interconnection of gaps also affect the permeability (Sant et al., 2011).

Fly ash is used to change the properties of concrete. The grain size in fly ash affects the performance of cement and concrete. For example, it increases strength, abrasion and freeze-thaw resistance in fly ash added concrete. The optimum grain size of fly ash has an effective role in the development of pozzolanic activity and in the compaction of concrete (Sevim and Demir, 2019).

In this study, fly ash taken from Afşin Elbistan thermal power plant was milled into fine grained material. Fly ash, of which different fineness values were obtained through grinding was substituted for cement in ratios of 10%, 30% and 50% by weight and reinforced concrete samples were produced. The effect of different fineness values and substitution ratios of fly ash used in concrete on the permeability of concrete was investigated. In this context, 28 and 90 days of capillary tests were performed to determine the permeability. As a result, it was found that the increase in the fineness of the fly ash and substitution rate decreased the permeability property.

2. Material and Method

2.1. Material

In this study, concrete samples were produced by using limestone aggregate, cement, fly ash and city water of Gümüşhane Municipality.

2.1.1. Aggregate

The aggregates used in the concrete composition were grouped as 0-4 mm, 4-11.2 mm and 11.2-22.4 mm. These aggregates were composed of limestones specific to Gümüşhane region (Fig. 1). Granulometry curves of the limestone aggregates used in the study are given in Fig. 2.

According to granulometry of the aggregate used in the study, curve A forms the representative curves showing the particle size distribution of aggregates with a dimension range of 11.2-22.4, curve B with a dimension range of 4-11.2 mm and curve C with a dimension range of 0-4 mm (Fig. 2).

2.1.2. Cement

CEM I 42.5 R type cement was used for the concretes produced in the study. This cement was supplied from Gümüşhane Aşkale cement factory. The specific physical, chemical and mechanical properties of the cement are given in Table 1.

Fig. 1. Limestone aggregate.

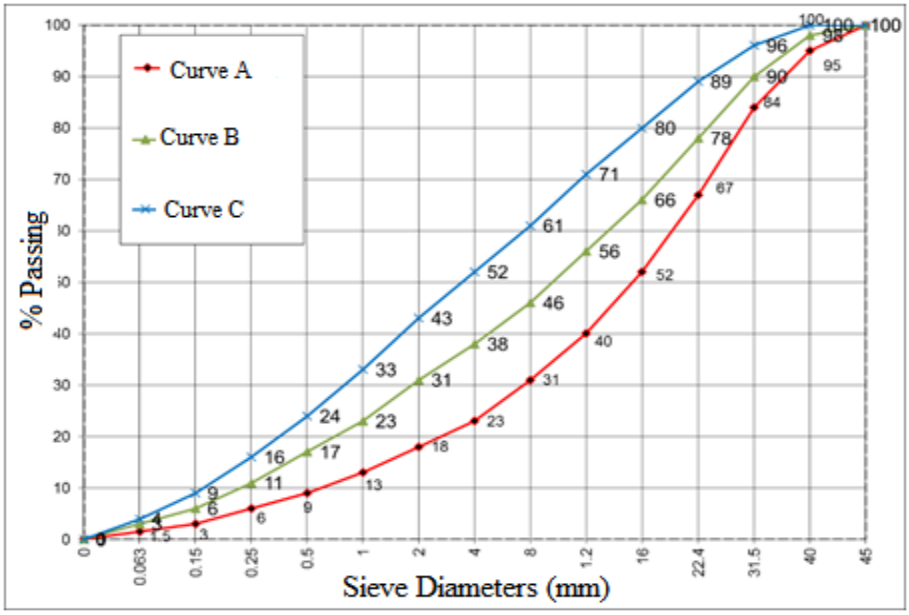

Fig. 2. Granulometric curves of aggregates according to TS 802 standard (TS 802, 2016).

Table 1. Properties of CEM I 42.5 R type cement.

Chemical Analysis (%)		Physical Tests	
SiO_2	18.59	Thinness (45 µ over the screen, %)	8.58
Al_2O_3	4.69	Specific Gravity (gr/cm^3)	3.08
Fe_2O_3	3.04	Blaine (cm^2/gr)	4145
CaO	60.34	Initial Setting (lllehour-min)	2hrs-33min
MgO	1.92	Final Setting (hour-min)	3hrs-18min
SO_3	2.89	Volume Expansion (mm)	0.7
Loss of ignition	7.19	Water Requirement (%)	29.9
Na_2O	0.11		
K_2O	0.64		
CI	0.0189	Compressive Strength (N/mm^2)	
Unmeasurable	0.57	2. day	23.9
Total	100	28. day	51.1
Free CaO	0.38		
Additive Content %	17.87		

The specific weight of the cement used was 3.08 gr/cm^3, its specific surface area was 4145 cm^2/gr and 8.58% over 45 μ sieve. According to the results of chemical analysis, ignition loss is 7.19%, free CaO 0.38%, SiO_2 18.59%, SO_3 2.89% (Table 1).

2.1.3. Fly ash

Fly ash was obtained from Afşin Elbistan thermal power plant in Kahramanmaraş Province. It is composed of unburned carbon grains in fly ash as shown in Fig. 3 and is dark brown. The physical and chemical properties of Afşin Elbistan fly ash were determined by performing the relevant experiments in the Gümüşhane Aşkale Cement Plant laboratory (Table 2).

According to ASTM C 618 standard; S+A+F (SiO_2 + Al_2O_3 + Fe_2O_3) sum was ≥70% and CaO<10% it was termed as class F (low level of lime), and if S+A+F (SiO_2 + Al_2O_3 + Fe_2O_3) sum was ≥50% and CaO>10% it was termed as C class (high level of lime) fly ash. According to this, Afşin Elbistan fly ash was S+A+F: 47.40%, CaO: 37.84%, and the amount of S+A+F in it was less than 50%, but since the CaO content was greater than 10% it was termed C class fly ash. Ignition loss was obtained as 2.31%, free CaO as 4.51% and 45 μ oversize as 50.68% (Table 2).

Fig. 3. A view of Afşin Elbistan fly ash.

Table 2. Chemical and physical properties of fly ash.

Chemical Analysis		Physical Tests	
Component,%	Fly Ash	Physical Properties	Components
SiO_2	29.24	Thinness (45 μ over the screen, %)	50.68
Al_2O_3	11.49		
Fe_2O_3	6.67	Specific Gravity (gr/cm^3)	2.54
CaO	37.84		
MgO	1.86	Specific Surface (cm^2/gr)	1834
Na_2O	0.38		
K_2O	0.69	Initial Setting (hour-min)	2hrs-30 min
SO_3	4.70		
Cr_2O_3	0.054	Final Setting (hour-min)	3 hrs-15 min
Mn_2O_3	0.059		
P_2O_5	0.494	Volume Expansion (mm)	0
TiO_2	0.49		
ZnO	0.001	Water Requirement (%)	27.4
KK	2.31		
Total	96.27	Water Content (gr)	137
Free CaO	4.51		

2.1.4. Mixing water

The water used for the construction of concrete samples consisted of city water belonging to Gümüşhane Municipality.

2.2. Method

In this study, concrete samples of C25 strength class were produced. Impermeability and capillarity values of these concrete samples were determined by being kept in curing pool up to 28 and 90 days.

The concrete produced in this study was designed according to the TS 802 standard and the samples given in Fig. 4 were produced.

2.2.1. Capillarity determination

100 x 200 mm cylinder concrete samples were removed from the curing pool at the end of the curing period of 28 and 90 days and allowed to dry for 3 days in an air circulation oven at 50±5°C. The lateral surfaces of the samples were then placed in a water-filled container with liquid-tight material (silicone), with 2±1 mm soles touching water. These samples were kept in water for 1, 5, 10, 20, 30, 60, 120, 180, 240, 300, 360, 600, 1440, 2280, 4320, 5760, 11520" min and their mass gains were determined by weighing up with a sensitivity value of 0.01 g. Capillary water absorption (CWA) values of concrete samples were calculated according to Eq. (1). The cumulative capillary water absorption values were plotted according to the square root of time. The amount of water absorbed by the

capillary concrete is directly proportional to the surface area and the square root of the elapsed time. The number *K*, which is proportionality constant and is also called the capillarity coefficient, is a property of the cavities of the concrete. The weight differences of the samples were calculated according to their initial weights and their CWA values were determined. Eq. (2) shown below was utilized used to calculate the capillarity coefficients. The capillarity coefficient was calculated to interpret the volumes of water leaking from each unit area (ASTM C 1585, 2013).

$$I = \frac{mt}{a/d} \tag{1}$$

In this equation;
I : Capillary water absorption (mm),
mt : the change in mass of concrete, for example, in time (t) grams
a : area of sample (mm^2) of concrete exposed to the test,
d : density of water ($gr\ mm^3$).

$$K = \frac{Q^2}{A^2 t} \quad (cm^2/sec) \tag{2}$$

In this equation;
K : Capillarity coefficient (cm^2/s),
a : Area in contact with water (cm^2),
t : Elapsed time (s),
Q : The amount of water absorbed is (cm^3).

Siliconization of the lateral surfaces of concrete samples used for capillarity testing (Fig. 5).

Examples of concrete dried in a drying oven and placed in a water-filled container for the capillarity test are shown in Fig. 6.

Measuring the mass changes as presented in Fig. 7 by removing the samples from the water-filled container at the end of the specified periods.

Fig. 4. Examples of fly ash added concrete.

Fig. 5. Siliconization of the samples to be tested for capillarity.

Fig. 6. Holding the concrete samples in the water filled container in the installed order.

Fig. 7. Measurement of mass changes at the specified time in the capillary test apparatus.

3. Results and Discussion

Capillarity test was performed in order to determine the permeability properties of reinforced concrete samples, produced by substituting Afşin Elbistan fly ash materials generated with different grinding times for cement. The results of the capillarity test performed on 28-day concrete samples with 10%, 30% and 50% fly ash substitution and the obtained capillarity coefficient values are given in Fig. 8.

It was observed that the increase of fly ash fineness in 10% fly ash added concrete samples reduces the permeability in concrete. The lowest water absorption rate of concrete with a substitution rate of 10% was determined as 0.76 mm for 60 min ground fly ash added concrete samples. The maximum amount of water absorption was calculated as 1.45 mm in the reference concrete sample. The concrete sample with a 60 min grinding time reduced the water permeability by about half by reducing it to -47% relative to the reference concrete (Fig. 8a). As a result of the refining of fly ash by grinding, it was seen that it forms more impermeable concretes by filling the gaps in concrete. Capillarity coefficient values decreased with increasing the grinding time according to the capillarity test result by filling the gaps in concrete. As shown in Fig. 8d, the lowest capillarity coefficient value among the 10% fly ash substitute concrete samples, i.e. the impermeable concrete sample, was determined as 8.45E-09 in the concrete sample having 60 min grinding time compared to the reference sample. The permeability value relative to the reference sample showed a decrease of -72.3%.

When the amount of fly ash substitution in concrete was increased to 30%, it exhibited a similar behavior with 10% fly ash substituted concrete and decreased the permeability value. The lowest water absorption rate was 0.75 mm in 60 min ground fly ash reinforced concrete samples and the maximum water absorption rate was 1.45 mm in reference concrete samples (Fig. 8b). 30% fly ash ground according to the reference sample reduced permeability by -46% in concretes. As shown in Fig. 8e, as the fly ash substitution rate and grinding time increased, the amount of water absorbed through the capillary channels in concrete decreased by about half.

When the fly ash substitution rate in concrete was increased to 50%, the amount of water absorbed by capillary channels was determined as 0.50 mm in the highest grinding time concrete sample and 1.4 mm in the reference sample (Fig. 8c). The fly ash reinforced concrete sample contributed to the formation of more impermeable concrete by absorbing - 66% less water than the ref-

erence sample. As shown in Fig. 8f, the capillarity coefficient value contributes to a significant reduction in permeability of approximately 80% and above in all milling time samples, except for a 50% unsaturated ash added concrete sample with respect to the reference sample. Fig. 9 shows the capillarity test results at the end of the 90-day curing period.

Capillary water absorption and capillarity coefficient values of Afşin Elbistan volatile reinforced concretes after 90 days curing period are given in Fig. 9. After the 90-day curing period, the highest water absorption value in Fig. 9a was observed in the concrete sample having a grinding time of 20 min as 3.24 mm. The water absorption value of the reference sample was determined as 1.94 mm, and the 67% fly ash added concrete sample had a higher water absorption value. The capillarity coefficient value was found to be 179.2% higher than the reference sample. The lowest water absorption value was observed in the concrete sample with 60 min grinding time, and the capillary water absorption value decreased by-3% and the capillarity coefficient value by -5,2% compared to the reference sample, causing the permeability to be reduced.

Capillary water absorption and capillary coefficient values of 30% substituted concrete samples are given in Figs. 9b and 9e. In Fig. 9b, the highest water absorption value is seen in the concrete reinforced sample with a grinding time of 45 min. The water absorption change in mm was 22% and the capillarity coefficient was 49.7% higher than the reference sample and it was found to be a more permeable concrete. The lowest water absorption value was -1,3% lower in the original fly ash reinforced concrete compared to the reference sample and it was more impermeable concrete.

Capillary water absorption and capillarity coefficient values of 50% substituted concrete samples are given in Fig. 9c and Fig. 9f. The highest water absorption value was 141% and capillarity coefficient increase was 483% higher in the concrete sample ground for 20 minutes compared to the reference sample and showed more permeable concrete properties. The lowest water absorption value was determined as the reference concrete sample.

Using Afşin Elbistan fly ash in concrete at different grinding times and substitution rates has greatly reduced the permeability after 28 days of curing time. In the 90-day concrete samples, water absorption values of concrete samples with some grinding times were calculated as higher than the reference. In general, according to the results of the capillarity test, fly ash contributes to decrease in the permeability of concrete. Shaikh and Supit (2015), in their study, maintained that fly ash reinforced concrete samples decreased permeability value by 6-11% compared to the unmixed samples. The properties revealed that the use of fly ash in concrete as high as 40% contributed greatly to reducing the permeability volume. As a result of the capillary water absorption test applied on concrete samples, the capillary water absorption coefficient of volatile ash concrete was found to be lower than those of unmixed concrete samples. As a result of their study, they concluded that fly ash reduces the permeability of cement paste and the transition zone around the aggregates and minimizes the permeability value of concrete. The effect of fly ash fineness and substitution rate on the permeability of concrete increases due to the increase in the fly ash's fineness, resulting in the formation of a tighter or gapless material by filling the voids. A gap-free material absorbs less water (Naganathan and Linda, 2013). It provides higher specific surface area compared to cement by fly ash grinding. In fly ash reinforced concretes with high specific surface area, the capillary cavities of the fly ash concretes were less and showed less water absorption properties since it reduces the volume of the binder and the thickness of the transition zone between the binder and aggregate (Saha, 2017). Fly ash reduces the risk of exiting calcium hydroxide with the C-S-H gels they form due to their pozzolanic properties and also reduces permeability. Fly ashes the porosity of concrete, regulates grain distribution by micro-aggregate effect and provides optimum compaction. Thus, they increase the resistance of concrete against external effects. In addition, due to its spherical and smooth surface structure, they increased the processability of fresh concrete (Unal and Uygunoglu, 2004).

That in the 90-day concrete samples reinforced with fly ash, capillarity value was higher compared to the reference sample stemmed from the fact that it had larger grain sizes than the cement. Since the pozzolanic activity in fly ashes develops in the long term, the grinding time up to 60 min for the development of pozzolanic activity was not sufficient to improve the pozzolanic activity of the fly ash. Furthermore, due to the grinding of fly ash, the round grain structure was disrupted and caused the formation of irregular grain structure. The deterioration of grain structure decreased the effect of filling the cavities and consequently caused an increase the porosity and permeability (Sinsiri et al., 2010).

Slowly filling the cavities with the hydration products during the hydration of the cement reduces the water permeability. Regarding the use of fly ash in the concrete composition and the development of pozzolanic reaction in the concrete, while fly ash reinforced concretes with the same water/binder ratio have more permeability in a short curing time compared to unmixed concrete, they have less permeability in a long curing time (Naik et al., 1994).

The permeability of concrete varies depending on water / cement ratio, crack structure, curing conditions and the type, fineness and quantity of mineral admixture. The effect of fly ash, which is one of the mineral additives and is widely used in concrete, on the permeability property varies according to grain size, grain shape, fly ash type and usage amount. Since the processability of the fly ash reinforced concretes formed of round grain structure increased, the water requirement of the mixture was reduced. However, due to the grain structure of the concretes prepared with the admixture of Afşin Elbistan ash having irregular grain structure, permeability in 28 days curing time was lower than that of reference concrete but permeability values of 90 days due to substitution rate and fineness were also higher (Bıparve, 2012).

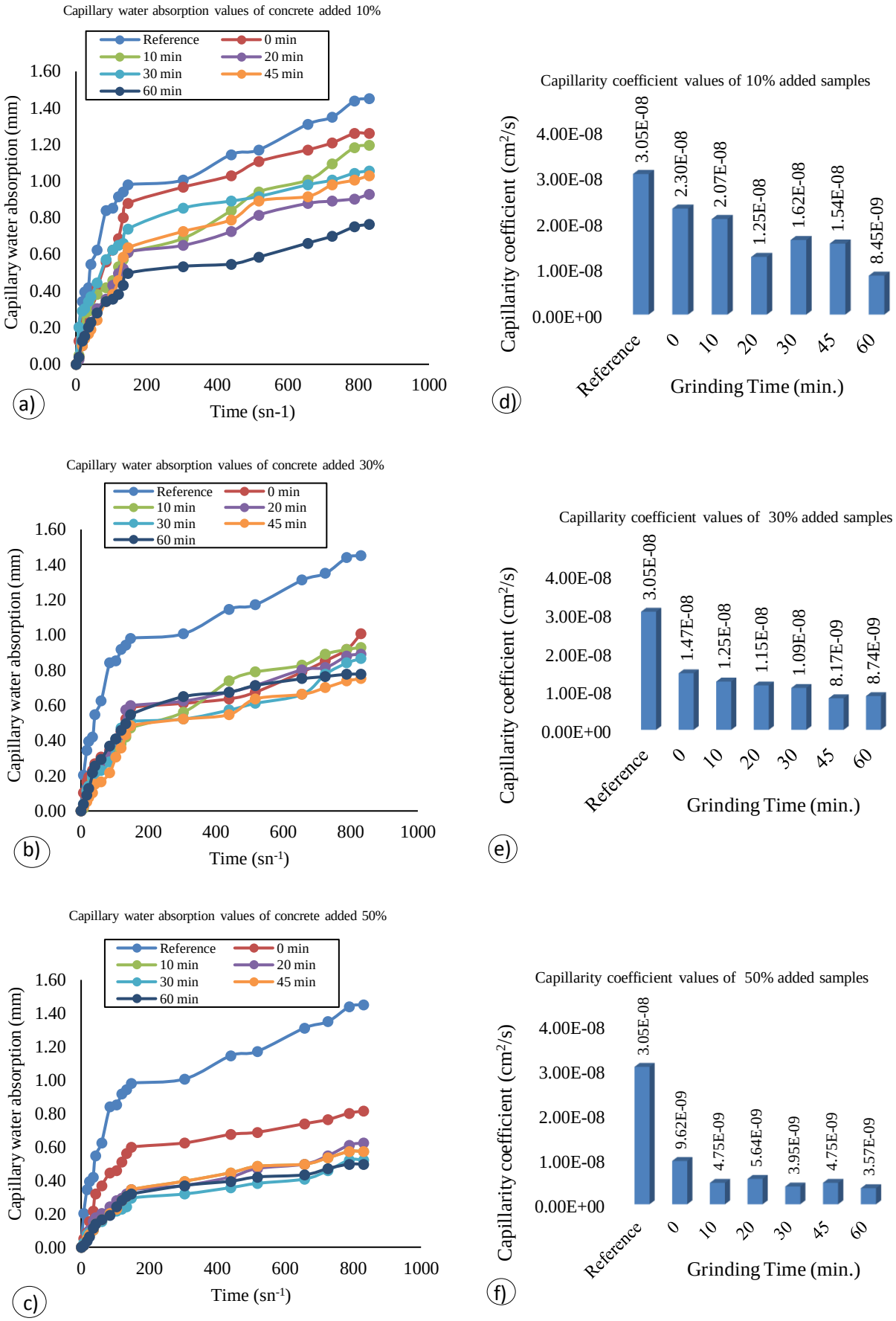

Fig. 8. Capillary water absorption and capillarity coefficient values of 28 days varying fly ash and substitution rate fly ash admixtures.

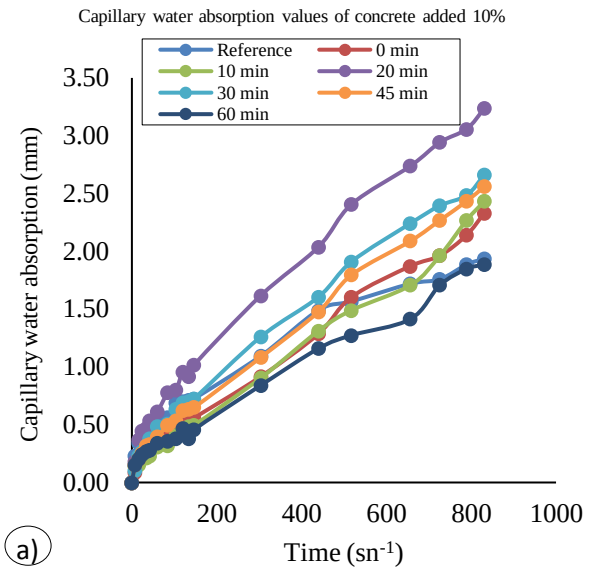

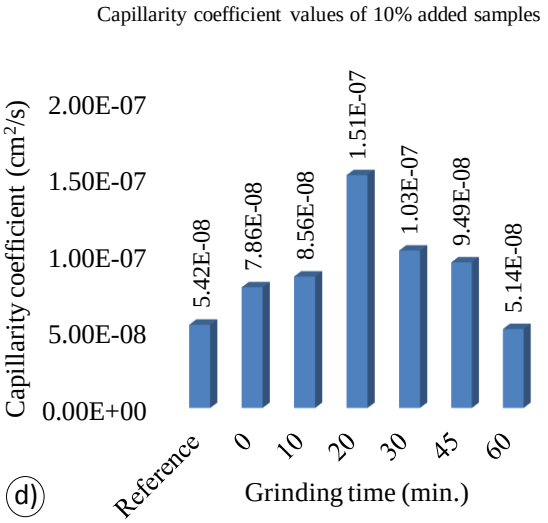

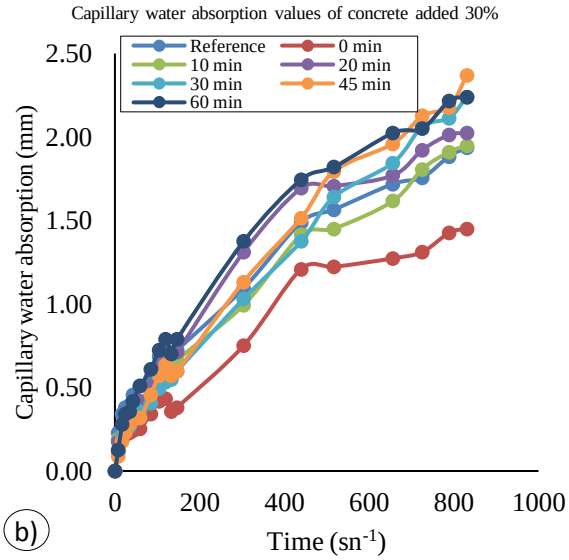

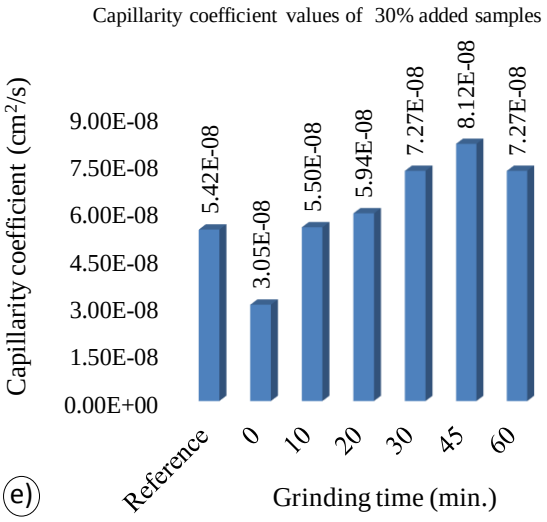

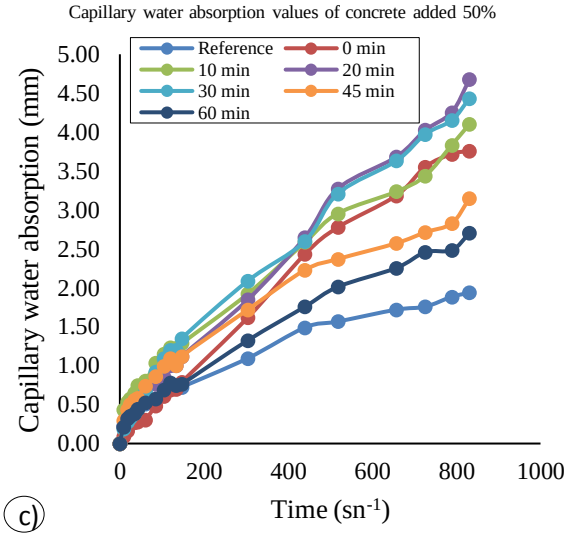

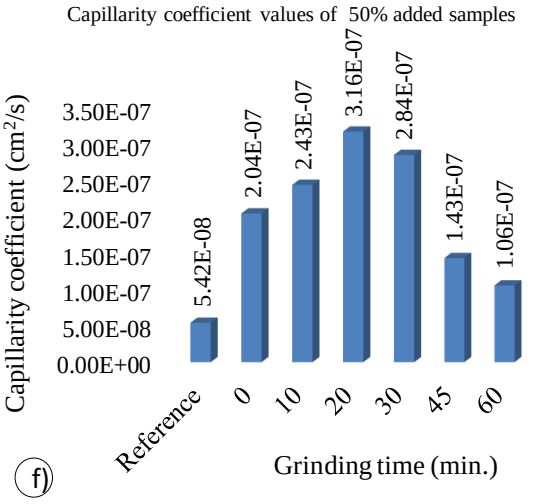

Fig. 9. Capillary water absorption and capillarity coefficient values of 90 days different fly ash and substitution rate fly ash admixtures.

In the study, after the curing period of 28 and 90 days, the differences between the samples obtained with different grain sizes of fly ash and the permeability value of the reference concrete showed differences from the connected cavities in the cement paste, micro cracks in the concrete, and the difference of the paste-aggregate interface. In particular, the voids and associated voids in the concrete are influenced by the water / cement ratio, the degree of hydration and the degree of compression. The different sizes of fly ashes caused a difference in the permeability properties of concrete samples since they affected the water / cement ratio, hydration degree and compression ratio. It consists of macro and micro crack system in concrete. In particular, the water permeability is determined by the capillary cavities. A cake's water / cement ratio and degree of hydration determine the total capillary voids (Mehta, 1990).

The particle size and distribution of aggregate in the concrete, the inner surface of the cement, the water / cement ratio, the degree of compaction of the fresh concrete, the curing condition, the humidity of the environment and the thermal history of the concrete are the factors affecting the micro-crack system of the concrete. With the use of fly ash of different Blaine fineness in concrete, it was aimed to change the microcrack structure of the concrete and to produce more impermeable concrete. Because permeability in concrete is determined by total porosity and distribution. In particular, permeability in concrete is associated with correlated voids. The fact that the concrete has a high void structure does not mean that it will have a high permeability; on the contrary it can show a low permeability. Sometimes concrete with low void structure can exhibit high permeability. The main reason for this situation is that the gaps are dependent and independent from each other. Therefore, the lack of void structure associated with fly ash reinforced concretes with a different fineness of 28 days caused low permeability compared to the reference. However, after 90 days curing period, that fly ash fineness was not effective on permeability stemmed from the formation of the correlative cavity structure (Chia and Zhang, 2002).

4. Conclusions

In this study, fly ash taken from Afşin Elbistan thermal power plant was milled into fine grained material. In the fly ash concrete, of which different fineness values were obtained by grinding was substituted for cement, in ratios of 10%, 30% and 50% by weight and reinforced concrete samples were produced. The effect of different fineness values and substitution ratios of fly ash used in concrete on the permeability property of concrete was investigated. In this context, 28 and 90 days of capillary tests were performed to determine the permeability. As a result;

- The amount of water absorbed by concrete samples prepared through capillary channels decreased as a result of the increase in the amount of fly ash in the concrete and the fineness with the effect of grinding.
- The reason for the decrease in capillary water absorption amount due to increase of fly ash ratio and fineness, decreased the amount of water absorbed by fly ash particles clogging the capillary channels.
- At the end of the 28-day curing period, the permeability values between the ground fly ash reinforced concrete samples and the reference sample were discussed more clearly. However, at the end of the 90-day curing period, the permeability values were close to each other in the ground concrete samples and the reference sample.
- In the 90 days fly ash reinforced concrete, $Ca(OH)_2$ and Si and Al compounds of fly ash formed as a result of cement hydration with fly ash reacted to form CSH and CAH structures. In these structures, they filled the gaps in the concrete and decreased permeability.
- Permeability in concrete changed, depending on variables such as the amount of binding material, water content, aggregate and grain distribution, curing conditions.
- Capillary cavities are not the only factors affecting water permeability in fly ash added concrete. However, the connection of capillary cavities is a critical factor in water permeability in unmixed and fly ash reinforced concretes.
- As a result of thinning of fly ash in terms of grain size, it decreased permeability by increasing pozzolanic activity and making the matrix more dense as a result of forming additional hydration products and increasing compressibility.
- Filling effect of fine-grained fly ashes, the development of pozzolanic activity due to fineness and cement hydration reduced the porosity and permability of the concrete thanks to the triple combination.
- The porosity and permability curing time of fly ash reinforced concretes were found to change in line with the fineness and substitution rate of the material. According to these parameters, the ideal substitution rate and fineness value of fly ash was at a level of 10% and 60 min grinding time, thus reducing permeability.
- That fly ash did not provide a significant reduction in permeability, especially during the 90-day curing time was associated with its not reaching the fineness of cement until 60 min of grinding time and not providing the ideal grain size. In addition, it did not contribute to the significant development of pozzolanic activity in the long cure period since it did not have the appropriate fineness value.

Publication Note

This research has previously been presented at the 3rd International Conference on Advanced Engineering Technologies (ICADET'19) held in Bayburt, Turkey, on September 19-21, 2019. Extended version of the research has been submitted to Challenge Journal of Structural Mechanics and has been peer-reviewed prior to the publication.

REFERENCES

ASTM C618-19 (2019). Standard specification for coal fly ash and raw or calcined natural pozzolan for use in concrete. *ASTM International,* West Conshohocken, PA.

ASTM C1585-13 (2013). Standard test method for measurement of rate of absorption of water by hydraulic-cement concretes. *ASTM International,* West Conshohocken, PA.

Bıparve A (2012). Permability and Durability Volume Fly Ash Concrete under an Applied Compressive Stress. *M.Sc thesis*, Shiraz University, Shiraz, Iran.

Bilir T, Gencel O, Topcu IB (2015). Properties of mortars with fly ash as fine aggregate. *Construction and Building Materials*, 93, 782-789.

Binici H, Görür EB, Durgun MY (2009). The use of Afşin-Elbistan fly ash and textile factory waste ash as pozzolanic admixture in concrete. *KSÜ Journal of Engineering Sciences*, 12(1), 10-19.

Chia KS, Zhang MH (2002). Water permeability and penetrability of high strength lightweight aggregate concrete. *Cement and Concrete Research*, 32, 639-645.

Hoffman GK (2006). Pozzolans and supplementary cementitious materials. *In Kogel JE, Trivedi NC, Barker JM and Krukowski ST*, *eds*. Industrial Minerals and Rocks 7th Edition, Society for Mining, Metallurgy and Exploration, Inc., Littleton, CO, 1161-1172.

Mehta PK (1990). Concrete: Structure, Properties, and Materials. Prentice Hall, New Jersey, USA.

Ministry of Energy and Natural Resources (MENR) (2018). Coal. Info Bank>Energy>Coal 2017. (http://www.enerji.gov.tr) (06.03.2018).

Naganathan S, Linda T (2013). Effect of fly ash fineness on the cement mortar. *Jordan Journal of Civil Engineering*, 7(3), 326-331.

Naik TR, Sing SS, Hossain MM (1994). Permeability of concrete containing large amounts of fly ash. *Cement and Concrete Research,* 24(5), 913-922.

Neville AM (1995). Properties of Concrete. 4th and final Ed., Longman's, London, UK.

Özcan İ, Bahadıroğlu C, Bozdoğan H (2014). Research on the reasons for the drying of planted saplings in the excavation areas around Afşin-Elbistan thermal power plant. *Nevşehir Journal of Science and Technology*, 3(1), 8-16.

Qiu JLQ, Xing F, Pan D (2014). Permeation properties and pore structure of surface layer of fly ash concrete. *Materials (Basel),* 7(6), 4282–4296.

Saha AK (2017). Effect of class F fly ash on the durability properties of concrete, *Sustainable Environment Research*, 28(1), 25-31.

Sant G, Bentz G, Weiss J (2011). Capillary porosity depercolation in cement-based materials: measurement techniques and factors which influence their interpretation. *Cement and Concrete Research*, 41(8), 854-864.

Sevim Ö, Demir İ (2019). Physical and permeability properties of cementitious mortars having fly ash with optimized particle size distribution *Cement and Concrete Composites*, 96, 266-273.

Shaikh FUA, Supit SWM (2015). High volume fly ash (HVFA) concretes containing ultrafine fly ash (UFFA), compressive strength and durability properties. *Construction and Building Materials*, 82, 192-205.

Sinsiri T, Chindaprasirt P, Jaturapitakkul C (2010). Influence of fly ash fineness and shape on the porosity and permeability of blended cement pastes. *International Journal of Minerals, Metallurgy and Materials,* 17(6), 683-690.

Toniolo N, Boccaccini AR (2017). Fly ash-based geopolymers containing added silicate waste. A Review. *Ceramics International*, 43(17), 14545-14551.

TS 802 (2016). Design concrete mixes. Turkish Standardization Institute, Ankara, Turkey.

Unal O, Uygunoğlu T (2004). Soma Termik Santral atığı uçucu külün inşaat sektöründe değerlendirilmesi. Turkey 14th Coal Congress, Zonguldak, Turkey (in Turkish).

Challenge Journal of Structural Mechanics

Research Article

The assessment of soil depth sensitivity to dynamic behavior of the Euler-Bernoulli beam under accelerated moving load

Amin Ghannadiasl [a,*], Hasan Rezaei Dolagh [a]

[a] *Department of Civil Engineering, University of Mohaghegh Ardabili, 56199-11367 Ardabil, Iran*

ABSTRACT

Dynamic behavior is one of the most crucial characters in the railways structures. One of the items which leads to precise identification of the dynamic behavior of railways is the soil depth beneath them. In this paper, an Euler-Bernoulli beam on a finite depth foundation under accelerated moving load is presented. The dynamic equilibrium in the vertical direction is only regarded in accordance with the factor of finite beams. In this study, the dynamic equilibrium of the soil in the vertical direction and the sensitivity of soil depth are considered. The governing equations are simulated by using Fourier transform method. Eventually, by considering the sequences of shear waves, and different kinds of damping, displacement of the beam is obtained for the various acceleration, times and soil depth. As a result, it is shown that, higher acceleration is not dramatically effective on the beam displacement. Also, foundation inertia causes a significant reduction in critical velocity and can augment the beam response.

ARTICLE INFO

Article history:
Received 22 November 2019
Revised 15 January 2020
Accepted 24 February 2020

Keywords:
Euler-Bernoulli beam
Accelerated moving load
Soil depth
Railway structure

1. Introduction

Dynamic behavior of structures under accelerated moving loads is an important field in engineering. Hence, a lot of researches are done in this case. Problems that are occurred by these kinds of loads cannot be neglected in the structures behavior. For instance, the displacement of the beam by considering speed and acceleration is effected by train force on the railways.

Several studies have been derived in the dynamic behavior of the beam under various types of loads. The initial research on the elastic foundation is performed by Timoshenko (1926). His work relates to the response of the railway under the constant speed of moving load. Kenney (1954) obtained a steady-state solution and showed that the critical velocity is really effective on the deformation of the beam. The frequency of the beam vibrations by using of finite element method was derived by Györgyi (1981). Li (2000) presented a simple and unified approach for analyzing the free vibration of the generally supported Euler-Bernoulli beam. The linear association of the Fourier series and an auxiliary polynomial function are used to specify the displacement of the desired beam. Hillal and Zibdeh (2000) recommended the vibration of the Euler-Bernoulli beam under moving load as a closed form solution. Also, an approach for extracting the dynamic behavior of damped Euler-Bernoulli beam excited by concentrated and distributed forces is provided by Abu-Hillal (2003). Kargarnovin and Younesian (2004) investigated the dynamic response of Timoshenko beam subjected to harmonic moving load with infinite length in the viscoelastic Pasternak foundation. Ying et al. (2008) studied the rough solutions for shear bending behavior and free vibration on the Winkler-Pasternak elastic foundation. Mehri et al. (2009) derived the dynamic behavior of the Euler-Bernoulli beam excited by moving load by using the Green function. Also, spectral analysis of the beam under the influence of load is recommended by Gladyzs and Sniady (2009). The desired beam is contemplated orthotropic at any point, whereas the properties of different materials in the thickness of beam are exponential. In addition, by using differential transform method the vibration of the Timoshenko and Euler-Bernoulli beam on elastic soil is predicted by

* *Corresponding author*. Tel.: +98-914-451-1813 ; Fax: +98-453-351-2910 ; E-mail address: aghannadiasl@uma.ac.ir (A. Ghannadiasl)
ISSN: 2149-8024 / DOI: https://doi.org/10.20528/cjsmec.2020.02.005

Balkaya et al. (2009). In this suggested method, accurate solutions without the serious analysis necessity are attained. Motaghian et al. (2011) investigated the problem of free vibration of the Euler-Bernoulli beam on the elastic foundation. Also, the nonlinear vibration of the Euler-Bernoulli beam with fixed ends under the influence of axial loads is derived by Barari et al. (2011), subjected to a bending load excitation while damping effect has been taken into account. A new analytical solution to predict the free lateral vibration of a Timoshenko beam with different kinds of boundary conditions is employed by Bazehhour et al. (2014). Also, the influence of the axial load on the natural frequencies is examined. Simultaneously, Prokić et al. (2014), illustrated a numerical approach to clarify the free vibration of Timoshenko beams with optional boundary conditions. The numerical approach is fundamentally attributed to numerical integration instead of the numerical differentiation. A proficient analytical approach to analyze the vibration of the Euler-Bernoulli beam on Winkler foundation is presented by Yayli et al. (2014). To attain the free vibration response of the beam on Winkler foundation, the Stoke's transformation with Fourier sine series is utilized. The dynamic response of the railway track structure subjected to moving load on visco-elastic foundation is derived by Mohammadzadeh and Mosayebi (2015). An analytical method and a combined finite element for predicting the vibration of a crane system subjected by suspended moving body is provided by Zrnić et al. (2015). Bian et al. (2016) presented the dynamic response of the railway under constant and accelerated moving loads with various velocities. For this purpose, the railways were modeled as the Euler–Bernoulli beam. Sheng et al. (2017) studied the dynamic response of the railways under the influence of moving harmonic load by using the Fourier transform method. By using the Green's function method, the dynamic behavior of the railway subjected to accelerated moving load investigated by Ghannadiasl (2017). Thereby, a direct and accurate modeling technique for railway is provided as the Euler-Bernoulli beam on the elastic foundation under the moving load with various boundary conditions. Ghannadiasl et al. (2018) investigated the dynamic analysis of the Euler-Bernoulli cracked beam on the elastic foundation under the concentrated load. Using Green's function natural frequency and deflection of Euler–Bernoulli beam with severel boundary conditions are obtained. Ghannadiasl et al. (2019) also carried out multi-span damped cracked beam by using the desired approach.

The dynamic behavior of the Euler–Bernoulli beam excited by the moving load in the previous studies is assessed. In present work, a precise solution in closed form is illustrated for assessing of soil depth sensitivity to dynamic behavior of the Euler-Bernoulli Beam under accelerated moving load. Also, it might be mentioned here that the previous authors did not provide the effects of time and soil depth for various foundations. The present paper is organized as follows. In section 2, the governing equations based on the Euler-Bernoulli beam theory is illustrated. Then, in section 3, the complete solutions and some numerical examples are provided. In section 4, effects of the soil depth, time and acceleration with some numerical examples are depicted. Finally, in section 5, the conclusions are classified, briefly.

2. Modelling of the Euler-Bernoulli Beam under Accelerated Moving Load

In present study, an infinite Euler-Bernoulli beam under of different kinds of damping coefficients like beam internal and viscous damping is studied as shown in Fig. 1. The governing differential equation of the Euler-Bernoulli beam is described as below:

$$\left(\frac{\partial^4}{\partial x^4}\left(EI + c_i\frac{\partial}{\partial t}\right) + N\frac{\partial^2}{\partial x^2} + m\frac{\partial^2}{\partial t^2} + c_b\frac{\partial}{\partial t}\right)w(x,t) + P_s = P\,\delta\left(x - X_F(t)\right) \quad (1)$$

where c_i is the beam internal damping coefficient, N is the axial force, which is assumed positive in compression, m is the beam mass per unit length, P_s is the pressure of foundation that will be switched later, P is the moving load, and v is its velocity. $w(x,t)$ and P show beam displacement and moving load respectively, which are presumed positive when acting downward. Moreover, δ is the Dirac delta function and c_b is the beam viscous damping coefficient.

The equation of the trajectory of the moving load, $X_F(t)$, is illustrated as:

$$X_F(t) = v_{0x}t + \frac{1}{2}a_{0x}t^2 \quad (2)$$

where v_{0x} is the initial speed of the moving load in the x direction, a_{0x} is the constant acceleration of the moving load in the x direction and t refers to time. This function can be described a uniform accelerating motion. On the other hand, the dynamic equilibrium of the soil in the vertical direction illustrated in terms of:

$$\bar{\rho}\left(v_{0x} + a_{0x}t\right)^2\frac{\partial^2 u}{\partial s^2} - c_f\left(v_{0x} + a_{0x}t\right)\frac{\partial u_r}{\partial s} = \bar{k}_{st}H\frac{\partial^2 u}{\partial z^2} + \bar{G}_s\frac{\partial^2 u}{\partial s^2} \quad (3)$$

where the upper bar illustrates the limitation to the finite strip b, in other words, density and moduli of soil are multiplied by b. u_r is the vertical soil displacement which is used in order to introduce the influence of foundation damping accurately, v is velocity of the load, $\bar{\rho}$ is soil density, $\bar{k}_{st}$ depicts the stiffness, H is soil depth, the expression $\bar{G}_s(\partial^2 y/\partial x^2)$ counts for the shear effect and c_f is the foundation viscous damping coefficient.

All variables will be utilized in dimensionless forms. The critical velocity will be specified by parametric analysis and the systems of Eqs. (1) and (3) will be clarified for steady-state beam deflection. Thereby, changing the equations to moving coordinate $s = x - vt$ and by considering limitation to the steady state conditions gives:

$$\left(EI - c_i\left(v_{0x} + a_{0x}t\right)\right)\frac{\partial^4 w}{\partial s^4} + \left(N + m\left(v_{0x} + a_{0x}t\right)^2\right)\frac{\partial^2 w}{\partial s^2} - \left(v_{0x} + a_{0x}t\right)c_b\frac{\partial w}{\partial s} + P_s = P\,\delta(s) \quad (4)$$

$$\bar{\rho}\left(v_{0x}+a_{0x}t\right)^2\frac{\partial^2 u}{\partial s^2}-c_f\left(v_{0x}+a_{0x}t\right)\frac{\partial u_r}{\partial s}=\bar{k}_{st}H\frac{\partial^2 u}{\partial z^2}+\bar{G}_s\frac{\partial^2 u}{\partial s^2} \quad (5)$$

Initially, the Eq. (4) is solved. Thereafter the relative displacement satisfies the boundary conditions, which makes the determination easier. Thereby

$$z=\zeta H\ ,u=u_r+\left(1-\zeta\right)w \quad (6)$$

where z is vertical axis, H is soil depth, u is the beam displacement.

Furthermore with $\chi=\sqrt[4]{\bar{k}_{st}/4EI}$, the moving coordinate s changes to dimensionless coordinate $\xi=\chi s$, and by dividing all terms by the static displacement $w_{st}=p\chi/2\bar{k}_{st}$, to attain dimensionless $\hat{u}_r$ and $\hat{w}$, gives:

$$\left(1-\left(\frac{\vartheta_s}{\alpha}\right)^2\right)\frac{\partial^2\hat{u}_r}{\partial\xi^2}-\frac{\eta_f}{\alpha\mu^2}\frac{\partial\hat{u}_r}{\partial\xi}-\frac{1}{\alpha^2\mu^2}\frac{\partial^2\hat{u}_r}{\partial\zeta^2}=-\left(1-\left(\frac{\vartheta_s}{\alpha}\right)^2\right)\left(1-\zeta\right)\frac{\partial^2\hat{w}}{\partial\xi^2} \quad (7)$$

where, $\vartheta_s=\frac{v_s}{v_{cr}}$ shows the shear coefficient which the term v_s in it, stands for the velocity of the shear waves, $\alpha=\left(v_{0x}+a_{0x}t\right)/v_{cr}$ is the velocity ratio with $v_{cr}=\sqrt[4]{\frac{4\bar{k}_{st}EI}{m^2}}$, μ is the mass ratio that explained as $\mu=\sqrt{\bar{\rho}H/m}$, and $\eta_f=\frac{c_f H}{\sqrt{\bar{k}_{st}m}}$.

According to the homogeneous conditions, the following relation can be presumed

$$\hat{u}_r=\sum_{j=r}^{\infty}U_j\sin\left(j\pi\zeta\right) \quad (8)$$

Thereafter multiplication with one mode shape, substitution and integration from 0 to 1 depth, and by Fourier transform yields:

$$U_j^*=\frac{\omega^2\frac{2}{j\pi}\left(1-\left(\frac{\vartheta_s}{\alpha}\right)^2\right)}{-\omega^2\left(1-\left(\frac{\vartheta_s}{\alpha}\right)^2\right)-i\omega\frac{\eta_f}{\alpha\mu^2}+\left(\frac{j\pi}{\alpha\mu}\right)^2}W^* \quad (9)$$

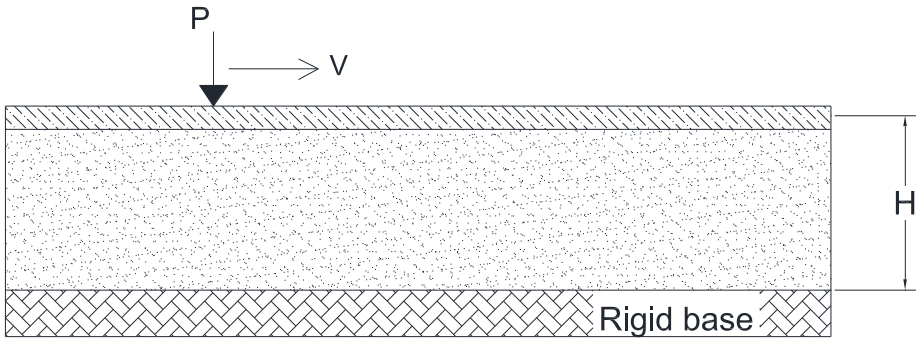

Fig. 1. The infinite beam on soil under accelerated moving load.

According to the foundation pressure as follows (Dimitrovová, 2016):

$$P_s=-\left(1-\mathrm{i}\eta_h\right)\bar{k}_{st}\left(\sum_{j=1}^{\infty}j\pi u_j-w\right) \quad (10)$$

where η_h illustrates the coefficient of the hysteretic damping and $u_j=U_j w_{st}$. Hence, getting back to Eq. (1), one attains

$$\left(EI-c_i\left(v_{0x}+a_{0x}t\right)\right)\frac{\partial^4 w}{\partial s^4}+\left(N+m\left(v_{0x}+a_{0x}t\right)^2\right)\frac{\partial^2 w}{\partial s^2}-c\left(v_{0x}+a_{0x}t\right)\frac{\partial w}{\partial s}-\left(1-i\eta_h\right)\bar{k}_{st}\left(\sum_{j=1}^{\infty}j\pi u_j-w\right)=P\,\delta(s) \quad (11)$$

Changes to dimensionless values, here moreover $\eta_i=2\alpha\chi c_i/2\sqrt{mEI}$, $\eta_N=N/2\sqrt{\bar{k}_{st}\left(EI-c_i v\right)}$ and $\eta_b=c_b/2\sqrt{m\bar{k}_{st}}$ are presented.

$$\left(1-\eta_i\right)\frac{\partial^4\hat{w}}{\partial\xi^4}+4\left(\left(\frac{\left(v_{0x}+a_{0x}t\right)}{v_{cr}}\right)^2+\eta_N\right)\frac{\partial^2\hat{w}}{\partial\xi^2}-8\eta_b\frac{\left(v_{0x}+a_{0x}t\right)}{v_{cr}}\frac{\partial\hat{w}}{\partial\xi}+4\left(1-i\eta_h\right)\left(\hat{w}-\sum_{j=1}^{\infty}j\pi U_j\right)=8\delta(\xi) \quad (12)$$

By the Fourier transform one acquires:

$$W^*=\frac{8}{\beta+4\left(1-i\eta_h\right)S} \quad (13)$$

and

$$\beta=\left(1-\eta_i\right)\omega^4-4\omega^2\left(\alpha^2+\eta_N\right)-8i\omega\eta_b\alpha+4\left(1-i\eta_h\right)$$

$$S=1+\sum_j\frac{\omega^2\frac{2}{j\pi}\left(1-\left(\frac{\vartheta_s}{\alpha}\right)^2\right)}{-\omega^2\left(1-\left(\frac{\vartheta_s}{\alpha}\right)^2\right)-i\omega\frac{\eta_f}{\alpha\mu^2}+\left(\frac{j\pi}{\alpha\mu}\right)^2} \quad (14)$$

3. Numerical Examples

An Euler–Bernoulli beam under a moving load is considered for the purpose of verification. The beam is expressed with the following features in Table 1.

Table 1. Numerical data.

Property	Case
Beam bending stiffness EI	$6.4(MN\,m^2)$
Beam mass per unit length m	$60(kg/m)$
Beam damping η_b	0.02
Soil Young's modulus $\bar{E}_s$	$10(MN\,m^{-1})$
Soil Poisson's ratio ν	0.2
Soil density $\bar{\rho}$	$185(kg/m^2)$
Active depth H	$1,4,8,12(m)$
Foundation damping η_f	0.629
Force P	$100(kN)$
Velocity v_{0x}	$323(m/s)$
Critical velocities v_{cr}^{E-B}	$325(m/s)$

Therefore, by assuming $\eta_i = a_{0x} = 0$, in Eq. (13), the governing equation for the Euler–Bernoulli beam gets as follow (Dimitrovová, 2016):

$$W^* = \frac{8}{\omega^4 - 4\omega^2\left(\alpha^2 + \eta_N\right) - 8i\omega\eta_b\alpha + 4(1 - i\eta_h)S} \tag{15}$$

In order to compare and justify various theoretical models with each other, such as classical Winkler foundation, the model without and with shear contribution, and classical Pasternak and visco-elastic foundations, deflection shapes for these mentioned cases are investigated and shown in Fig 2. By using the presented values, Eq. (13) and by introducing $\vartheta_s = 0$ and $\mu = 0$, solution for classical Winkler's foundation; for $\vartheta_s = 0$ model without shear contribution, for $\mu = 0$ solution for classical Pasternak foundation, and for $\eta_h = 0.529$ model for visco-elastic foundation are attained.

According to the Fig 2, it can be seen that the occupied large area with superior displacement behind the load, stands for the solution without shear contribution. That is because of the vibration of not interacted soil columns. The classical solution for Pasternak, Winkler and visco-elastic foundations provided very low displacement, because the applied velocity is approximately far from the critical one.

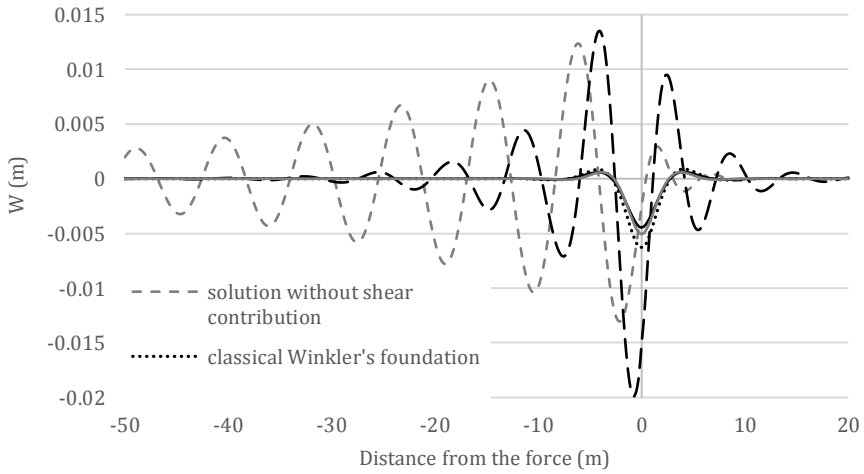

Fig. 2. Deflection shapes comparison for presented values.

On the other hand, the assessment of the critical velocity is shown in Figs. 3 and 4 by deriving the maximum downward and upward displacements. The graphs in Figs 3 and 4 depict that there is rarely any displacement directed upward and downward under the critical velocity. Both of the displacements over the critical velocity, for classical Winkler foundation, the model without and with shear contribution, classical Pasternak foundation, and visco-elastic foundation are compared.

4. Effect of Soil Depth, Time and Acceleration

Analysis of the soil depth and various types of damping are illustrated in this section. The soil depth is surely effective on the dynamic behavior of the beam. So, displacement shapes for different values of active depth ($H = 5,7,10,15m$) are obtained in Figs. 4 and 5. From the figures it is seen that by increasing the soil depth, the displacement of the beam is decreased for both solutions i.e. solution with and without shear contribution. In contrary, the displacement shapes for classical Winkler's foundation, classical Pasternak's foundation and visco-elastic foundation does not changes by increasing of the soil depth because of the value of shear ratio $\mu = 0$.

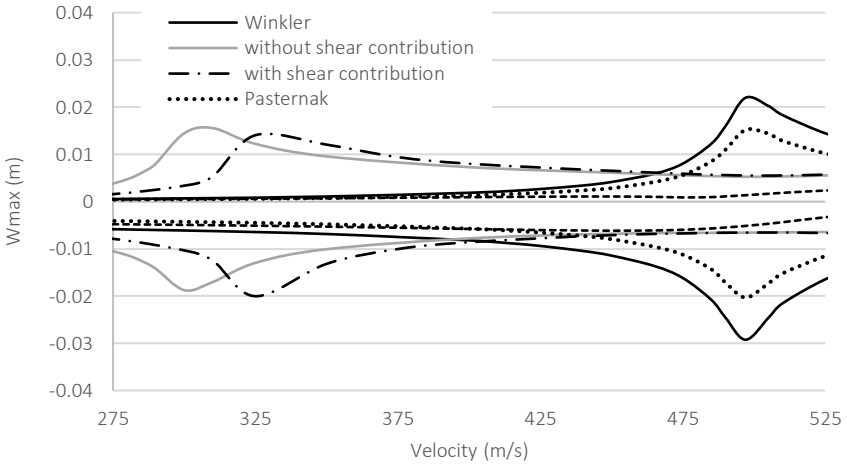

Fig. 3. Maximum displacements directed downward and upward.

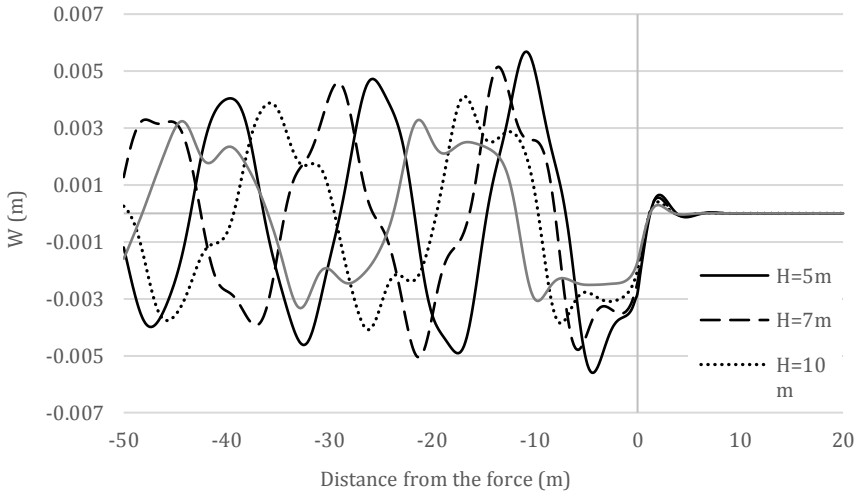

Fig. 4. Displacement shapes for various values of the soil active depth: solution with shear distribution.

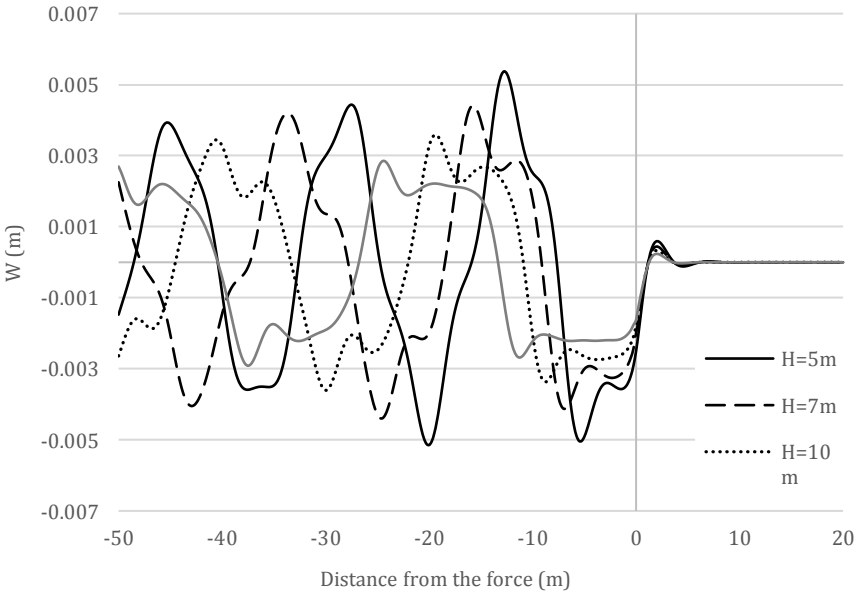

Fig. 5. Displacement shapes for various values of the soil active depth: solution without shear distribution.

As the matter of fact, two factors i.e. acceleration and time play an important role in dynamic behavior of the beam. Therefore, the influence of these two factors on displacement shapes of the beam are provided in Figs. 6 and 7. From Fig. 6 can be seen that by increasing the acceleration of the moving load the displacement of the beam decreases, but when the acceleration soars up to $2000\,\mathrm{m/s^2}$, the displacement of the beam gets stable and approximately reaches zero. Incidentally, according to the Fig. 7, by increasing the time the displacement of the beam decreases.

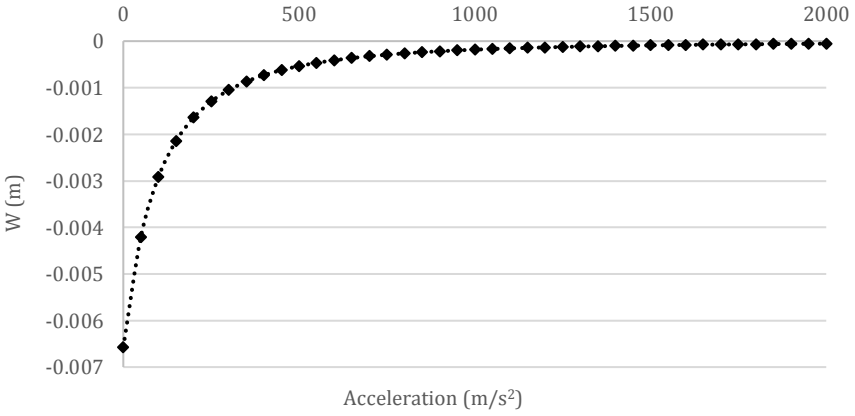

Fig. 6. Displacement shape for various values of the acceleration on Winkler foundation.

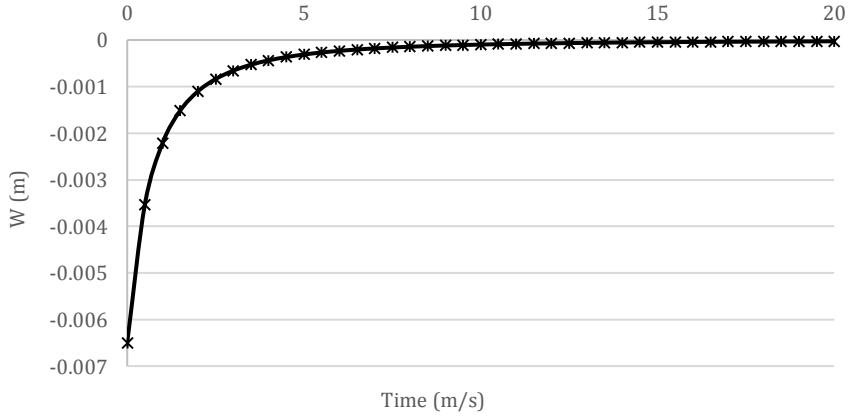

Fig. 7. Displacement shape for various values of the time on Winkler foundation.

5. Conclusions

In this paper, the Euler-Bernoulli beam was analyzed on the various depth of foundation under accelerated moving load and the displacement shapes for different values of active depth were provided. It was shown that the depth of soil is surely effective on the dynamic behavior of the beam. By increasing depth of soil, the displacement of the beam is decreased. On the report of the obtained graphs, it was identified that the occupied large area with superior displacement behind the load stands for the solution without shear contribution. That is because of the vibration does not interacted the soil columns. The classical solution for Pasternak, Winkler and visco-elastic foundations provide very low displacement, because the applied velocity is approximately far from the critical one. It was also declared that, by increasing the acceleration and time zone, the displacement of the beam is decreased. Also, the maximum displacement occurred when the acceleration zone and time are zero.

Publication Note

This research has previously been presented at the 3rd International Conference on Advanced Engineering Technologies (ICADET'19) held in Bayburt, Turkey, on September 19-21, 2019. Extended version of the research has been submitted to Challenge Journal of Structural Mechanics and has been peer-reviewed prior to the publication.

References

Abu-Hilal M (2003). Forced vibration of Euler–Bernoulli beams by means of dynamic Green functions. *Journal of sound and vibration*, 267(2), 191-207.

Balkaya M, Kaya MO, Sağlamer A (2009). Analysis of the vibration of an elastic beam supported on elastic soil using the differential transform method. *Archive of Applied Mechanics*, 79(2), 135-146.

Barari A, Kaliji HD, Ghadimi M, Domairry G (2011). Non-linear vibration of Euler-Bernoulli beams. *Latin American Journal of Solids and Structures*, 8(2), 139-148.

Bazehhour BG, Mousavi SM, Farshidianfar A (2014). Free vibration of high-speed rotating Timoshenko shaft with various boundary conditions: effect of centrifugally induced axial force. *Archive of Applied Mechanics*, 84 (12), 1691-1700.

Bian X, Cheng C, Jiang J, Chen R, Chen Y (2016). Numerical analysis of soil vibrations due to trains moving at critical speed. *Acta Geotechnica*, 11(2), 281-294.

Dimitrovová Z (2016). Critical velocity of a uniformly moving load on a beam supported by a finite depth foundation. *Journal of Sound and Vibration*, 366, 325-342.

Ghannadiasl A (2017). Analytical study of dynamic response of railway on partial elastic foundation under travelling accelerating concentrated load. *International Journal of Transportation Engineering*, 4(4), 317-334.

Ghannadiasl A, Khodapanah Ajirlou S (2018). Dynamic response of multi-cracked beams resting on elastic foundation. *International Journal of Engineering*, 31(11), 1830-1837.

Ghannadiasl A, Khodapanah Ajirlou S (2019). Forced vibration of multi-span cracked Euler–Bernoulli beams using dynamic Green function formulation. *Applied Acoustics*, 148, 484-494.

Gładysz M, Śniady P (2009). Spectral density of the bridge beam response with uncertain parameters under a random train of moving forces. *Archives of Civil and Mechanical Engineering*, 9(3), 31-47.

Györgyi J (1981). Frequency-dependent geometrical stiffness matrix for the vibration analysis of beam systems. *Periodica Polytechnica Civil Engineering*, 25(3-4), 151-163.

Hilal MA, Zibdeh HS (2000). Vibration analysis of beams with general boundary conditions traversed by a moving force. *Journal of Sound and Vibration*, 229(2), 377-388.

Kargarnovin MH, Younesian D (2004). Dynamics of Timoshenko beams on Pasternak foundation under moving load. *Mechanics Research Communications*, 31(6), 713-723.

Kenney JT (1954). Steady-state vibrations of beam on elastic foundation for moving load. *Journal of Applied Mechanics.* 21, 359-364.

Li WL (2000). Free vibrations of beams with general boundary conditions. *Journal of Sound and Vibration*, 237(4), 709-725.

Mehri BA, Davar A, Rahmani O (2009). Dynamic Green function solution of beams under a moving load with different boundary conditions. *Scientia Iranica - Transaction B, Mechanical Engineering*, 273-279.

Mohammadzadeh S, Mosayebi SA (2015). Dynamic analysis of axially beam on visco-elastic foundation with elastic supports under moving load. *International Journal of Transportation Engineering*, 2(4), 289-296.

Motaghian SE, Mofid M, Alanjari P (2011). Exact solution to free vibration of beams partially supported by an elastic foundation. *Scientia Iranica - Transaction A, Civil Engineering*, 18(4), 861.

Prokić A, Bešević M, Lukić D (2014). A numerical method for free vibration analysis of beams. *Latin American Journal of Solids and Structures*, 11(8), 1432-1444.

Sheng X, Zhong T, Li Y (2017). Vibration and sound radiation of slab high-speed railway tracks subject to a moving harmonic load. *Journal of Sound and Vibration*, 395, 160-186.

Timoshenko S (1926). Method of analysis of statical and dynamical stresses in rail. *Proceedings of the Second International Congress for Applied Mechanics, Zurich Switzerland*, 407-418.

Yayli MÖ, Aras M, Aksoy S (2014). An efficient analytical method for vibration analysis of a beam on elastic foundation with elastically restrained ends. *Shock and Vibration*, 2014.

Ying J, Lu CF, Chen WQ (2008). Two-dimensional elasticity solutions for functionally graded beams resting on elastic foundations. *Composite Structures*, 84(3), 209-219.

Zrnić NĐ, Gašić VM, Bošnjak SM (2015). Dynamic responses of a gantry crane system due to a moving body considered as moving oscillator. *Archives of Civil and Mechanical Engineering*, 15(1), 243-250.

Challenge Journal of Structural Mechanics

Research Article

Investigation of influence of concrete material models on cyclic inelastic response of a concrete filled composite plate shear wall

Erkan Polat [a,*]

[a] *Department of Civil Engineering, Munzur University, 62000 Tunceli, Turkey*

ABSTRACT

A previously benchmarked finite element model of a previously tested composite plate shear wall-concrete filled (C-PSW/CF) was used to investigate the influence of three concrete material models on in-plane cyclic inelastic wall response, using LS-Dyna. The concrete material models considered were the Winfrith, KCC and CSCM, all available in LS-Dyna. Wall moment hysteresis, using the three concrete material models, were obtained and compared. Individual contribution of the steel and concrete to total base moment was investigated for each wall with the three concrete material models. The numerical results obtained using the KCC and CSCM were compared against the benchmarked results obtained using the Winfrith concrete material model. Moment contribution of the steel web and the steel boundary on total base moment of the steel part of the wall and moment contribution of the concrete web and concrete boundary on total base moment of the concrete part of the wall were individually investigated. The wall models with the KCC and CSCM concrete models were observed to cannot capture wall pinching which was captured by the Winfrith concrete model. The wall strength was overpredicted by the CSCM concrete model and predicted reasonably by the KCC concrete model. Average axial stress distribution of the infill concrete was obtained to investigate wall neutral axis and the maximum attained concrete strength using the three concrete models. Concrete axial stress distribution showed some level of confinement for the concrete models considered.

ARTICLE INFO

Article history:
Received 20 November 2019
Revised 25 December 2019
Accepted 8 January 2020

Keywords:
Concrete filled composite plate shear wall
Cyclic response
Finite element analysis
LS-Dyna

1. Introduction

Composite plate shear wall–concrete filled (C-PSW/CF) consists of steel skin plates filled with concrete (AISC 2016). C-PSW/CF can be used with or without boundary elements. The boundary elements can consist of either circular or half-circular concrete filled tubes as stipulated by AISC (2016). In C-PSW/CF steel web plates are interconnected (in the transverse direction) by tie bars that are distributed at a specified spacing along the width and height of the wall. Tie bars help stabilize the empty wall module during construction and provide resistance for the concrete casting pressure. Additionally, the steel-concrete composite action is achieved by the shear and axial force transfer at the steel-concrete interface by the tie bars.

C-PSW/CF is a promising alternative to conventional reinforced concrete shear walls. It offers advantages in terms of construction cost and time (steel plates are prefabricated and allows modular construction on site). For this type of shear walls, steel modules provide formwork, and at the same time serve as falsework (Varma et al., 2019). Outer steel modules provide reinforcement (in both transverse and longitudinal direction) so that shear and flexural rebar usage are eliminated (helps speed up the construction schedule and reduce on-site labor for any rebar related work). This type of shear walls has high flexural capacity and ductility, and popular in mid-rise to high-rise buildings located in seismic regions (Polat and Bruneau, 2017). These type of wall systems have been used in some high-rise buildings, including Rainer Square Tower in Seattle, China World Trade Center.

* *Corresponding author*. Tel.: +90-428-213-1794 ; E-mail address: erkanpolat@munzur.edu.tr (E. Polat)
ISSN: 2149-8024 / DOI: https://doi.org/10.20528/cjsmec.2020.02.006

Finite element methods have been widely used to investigate C-PSW/CF for their seismic performance. Advanced finite element programs, such as ABAQUS (Hibbett et al., 2011) and LS-Dyna (LSTC, 2013) are some of the mostly used commercially available programs. Polat and Bruneau (2017, 2018), Epackachi et al. (2015), Kurt et al. (2016) used LS-Dyna to replicate experimentally obtained wall behavior such as wall base shear–top displacement hysteresis. Most of the numerical studies conducted previously employed limited number of concrete material models. A comparative study using different concrete material models for C-PSW/CF is limited. It is of interest to investigate the wall behavior using other concrete material models available in the programs. The focus of the study is to evaluate the significance of different concrete material models by using a previously benchmarked planar C-PSW/CF with boundary elements. The concrete material models considered are Mat085 (Winfrith), Mat072R3 (KCC) and Mat159 (CSCM) (all available in LS-Dyna). These concrete models are popular in structural modeling and simple to use.

2. Description of Reference Wall

The reference wall under consideration is shown in Fig. 1(a-b), where part (a) shows the wall cross-section and dimensions, and; part (b) shows the partial elevation of the wall base. Note that this wall model is one of the four walls tested and experimentally investigated by Alzeni and Bruneau (2017) (referred as B2 in that study). (Note that, in those four wall models, two had full circular boundary elements, and two had half-circular boundary elements. This study aimed to study behavior a wall with full circular boundary elements — with no other selection criteria). The wall was cantilever type and had a length of 3048mm from the base. As shown in Fig. 1(a) the wall consisted of circular boundary elements (HSS sections with a diameter of 219mm and thickness of 7.94mm) and dual steel web plates extending between the boundary elements (web plates had a thickness of 7.94mm and a width of 203.2mm). The inside volume of the circular boundary elements and dual web plates were filled with concrete (the thickness of the concrete between the steel web plates was 152.4mm). Tie bars (having a diameter of 25.4mm) were used to connect the dual web plates in the transverse direction. The vertical and horizontal spacing of tie bars was 304.8mm.

3. Theoretical Wall Strength and Plastic Neutral Axis Location

C-PSW/CF is assumed, theoretically, to reach its plastic moment capacity which is defined based on the assumption of uniform uniaxial yield strength of steel and uniaxial compressive strength of concrete (AISC, 2016). Fig. 2 shows the wall cross-section along with the assumed uniform plastic stress distributions of the skin steel and concrete. For fully plastic stress distribution, the skin steel is assumed to reach yield stress of F_y in compression and tension, and the concrete is assumed to reach compression stress of f_c'. Plastic moment capacity of the wall is given by the summation of the moments of the compressive and tensile force vectors about wall plastic neutral axis. The tensile and compressive force vectors are denoted by T_1, T_2, C_1, C_2, C_3, C_4, C_5 and shown in Fig. 2. In Fig. 2, the wall plastic neutral axis is defined based on a parameter C which can be calculated by equilibrium of compressive and tensile force vectors.

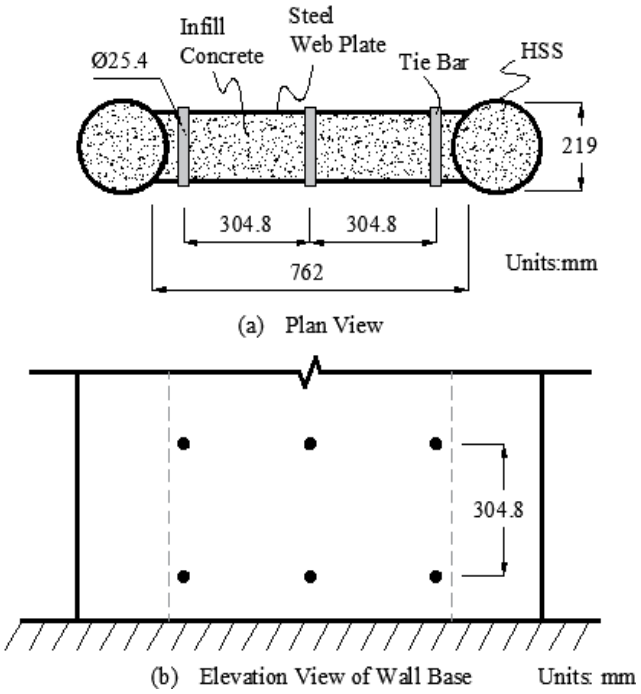

Fig. 1. Reference C-PSW/CF:
a) Plan view; b) Elevation view of wall base.

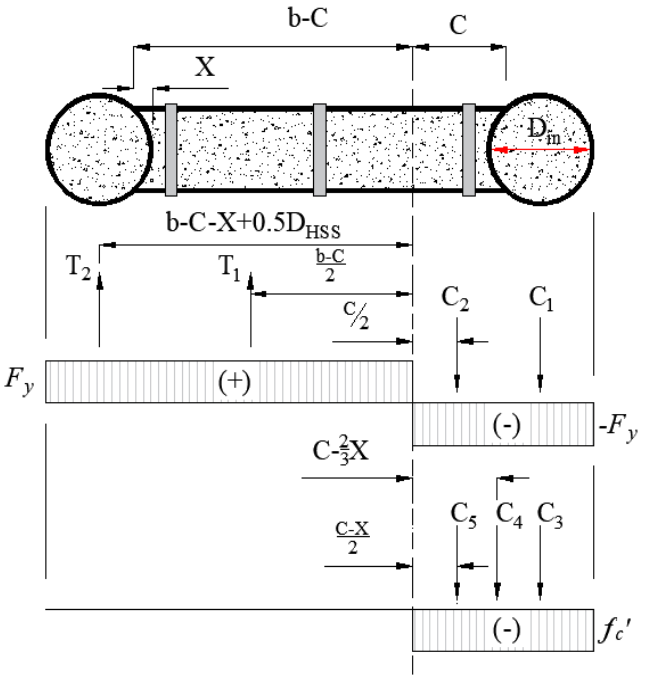

Fig. 2. Uniform stress distribution of steel and concrete part of the wall cross-section.

A closed-form solution for wall plastic moment, M_p, and plastic neutral axis, C, were provided by AISC (2016) and given in Eqs. (1) and (2). In these equations, A_{HSS} is the area of the HSS, F_{yHSS} and F_{yweb} are, respectively, the yield strength of the HSS and the steel web, d_{HSS} and d_{in} are, respectively, the outer and inner diameter of the HSS section, t_c and t_s are, respectively, the thickness of the infill concrete and steel. In Eq. (2), an auxiliary parameter, X, defined in closed form by Eq. (3), is used. Theoretical solutions using Eqs. (1) and (2) yield a value of M_p=3280 kN-m, and a C value of about 180mm. Including the partial depth of the HSS (≈180mm), a total compression depth is equal to about 360mm.

$$M_{pc} = M_n = A_{HSS}F_{yHSS}(b - 2X + d_{HSS}) + (b^2 + 2C^2 - 2Cb)t_sF_{yweb} + \left[0.25\pi d_{in}^2(0.5d_{HSS} + C - X) + 0.33Xt_c(C - 0.67X) + 0.5t_c(C - X)^2\right]f_c' \quad (1)$$

$$C = \frac{2bt_sF_{yweb} - \left(0.25\pi d_{in}^2 - 0.67Xt_c\right)f_c'}{4t_sF_{yweb} + t_cf_c'} \quad (2)$$

$$X = 0.5\left(d_{in} - \sqrt{d_{in}^2 - t_c^2}\right) \quad (3)$$

4. Finite Element Modeling of the Wall in LS-Dyna

Finite element modeling of the above-mentioned wall was previously developed by Polat and Bruneau (2017). Important modeling aspects are summarized as follows: shell, solid and beam elements were used to develop wall parts, namely; the steel plate, infill concrete and tie bars. Steel-concrete surface interaction was achieved by using a penalty-based contact model with interface friction (a coefficient of friction of 0.3 was used per the Coulomb friction model used by the contact model). Element sizes were determined based on a mesh convergence study. The size of the shell element was 25.4mm x 25.4mm and the solid elements was 25.4mm x 25.4mm x 25.4mm.

For modeling the concrete part of the wall, an eight-node constant stress solid element (Solid 1) with reduced integration was used. For modeling the steel part of the wall, a four node fully integrated shell element (Shell 16) with three integration points (through the thickness) was used. For modeling the ties, a two-node integrated beam element (Beam 1) was used. Fig. 3 shows the element mesh of the wall separately for the concrete infill (solid elements), tie bars (beam elements) and the steel skin (shell elements).

The material models used (as defined in LS-Dyna) in the finite element models were as follows: Mat 3, a bilinear material model with kinematic hardening, was used to define material properties of the steel plates and tie bars. The steel material properties used for the web plate and boundary elements (HSS) are as follows: Elastic modulus of E_s=205000MPa and 189000MPa, yield strength of F_y=441MPa and 386MPa, tangent modulus of E_t=100MPa and 413Mpa, respectively for the steel web plate and HSS. For tie bars, the same material model was used, except that F_y=345MPa and E=200000MPa. Three concrete material models, namely; Mat072R3 (Winfrith), Mat085 (KCC) and Mat159 (CSCM) were considered. The required input parameters with corresponding values for these concrete models are: concrete density of ρ=2.248e-008 N/mm^3, elastic modulus of 16,547 MPa, Poisson's ratio of 0.2, uniaxial concrete compressive strength of f_c'=49MPa, uniaxial tensile strength of f_t'= 4.9MPa and aggregate size of 7.9mm.

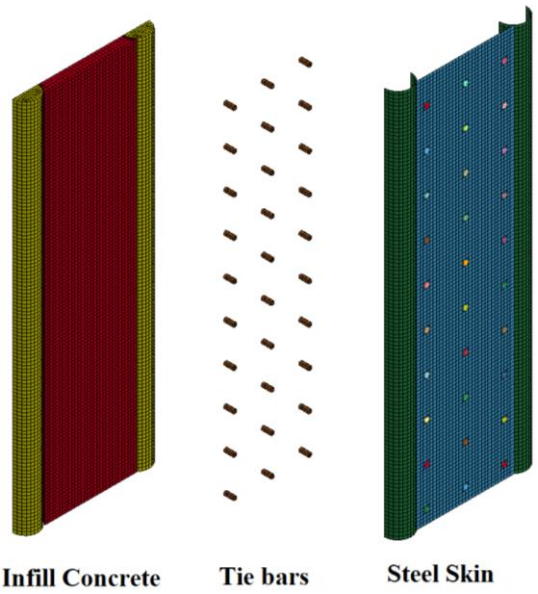

Fig. 3. Finite element model of the wall parts in LS-Dyna.

5. Comparison of Inelastic Cyclic Wall Responses

Cyclic wall responses were obtained by subjecting walls to displacement cycles at the wall top (displacement protocol was provided in Polat and Bruneau (2017)). Base moment – drift hysteresis, of the wall with different concrete material models were obtained and compared. Note that cyclic inelastic response of this wall was previously benchmarked by Polat and Bruneau (2017) using the Winfrith (Mat085) concrete model (in that study many wall response were successfully captured, such as; wall stiffness, strength and pinching). In this study, cyclic inelastic response of the same wall was investigated using the KCC and CSCM concrete models and the results are compared against the benchmarked results.

Figs. 4 and 5 show the comparison of the moment hysteresis curves obtained for the wall with the Winfrith, KCC and CSCM concrete models. As shown in Fig. 4, the moment hysteresis curve obtained using the KCC concrete model is in good agreement with that of the Winfrith concrete model in terms of wall stiffness and strength. As shown in Fig. 5 for the wall with the CSCM concrete model, wall strength and stiffness were over-predicted compared to those predicted using the Winfrith concrete model. The prediction of the wall pinching, however, was not captured successfully by the KCC and CSCM concrete models. Overall, the response obtained with the KCC concrete model is more reasonable than that obtained with the CSCM concrete model, and in better agreement with the benchmarked results obtained with using the Winfrith concrete model.

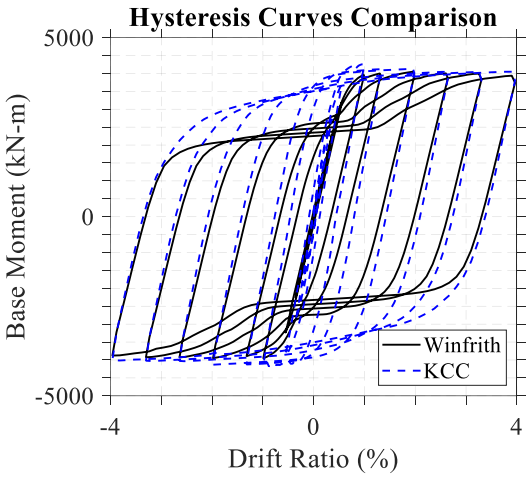

Fig. 4. Comparison of moment hysteresis of the wall with Winfrith and KCC concrete models.

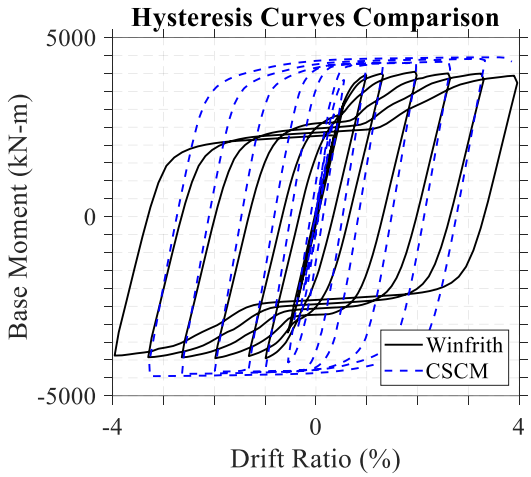

Fig. 5. Comparison of moment hysteresis of the wall with Winfrith and CSCM concrete models.

6. Investigation of Steel and Concrete Contribution to Total Wall Base Moment

Individual stiffness (lateral) and strength contribution of the steel and concrete of the wall models with the three concrete material models were investigated. Figs. 6-8 show the individual moment contribution of the steel (a), and concrete (b) to total base moment. Hysteresis curves in these figures show that contribution of the concrete and steel to total base moment varies for each concrete material model considered. For example, at 2.0% drift ratio steel contribution accounts for 73%, 64% and 63% of the total wall moment, while concrete contribution accounts for 27%, 36% and 37% of the total wall moment for the walls using the Winfrith, KCC and CSCM concrete models, respectively.

For the wall with the Winfrith concrete model (Fig. 6), the contribution of the steel to total wall strength is slightly reduced with increasing drift levels, whereas the contribution of concrete is slightly increased. This behavior is attributed to formation of local plate buckling on the steel web and HSS. Moreover, concrete contribution to stiffness is delayed as shown in Fig. 6(b) as a result of concrete cracking. Note that wall stiffness is related to wall pinching. Polat and Bruneau (2018) showed that wall pinching in flexural type C-PSW/CF was a result of concrete crack opening and closing. For the wall with the KCC concrete model (Fig. 7), similar to the wall with the Winfrith concrete model, there is slight reduction in steel strength and slight increase in concrete strength with increasing wall drift. Note that KCC concrete does not simulate concrete crack opening and closing therefore wall pinching cannot be captured with this material model. For the wall with the CSCM concrete model (Fig. 8), steel and concrete contribution to total wall moment differs from that of the walls with the Winfrith and KCC concrete models. For this wall the reduction in steel contribution and increase in concrete contribution with increasing wall drifts is more significant than that obtained using the Winfrith concrete model.

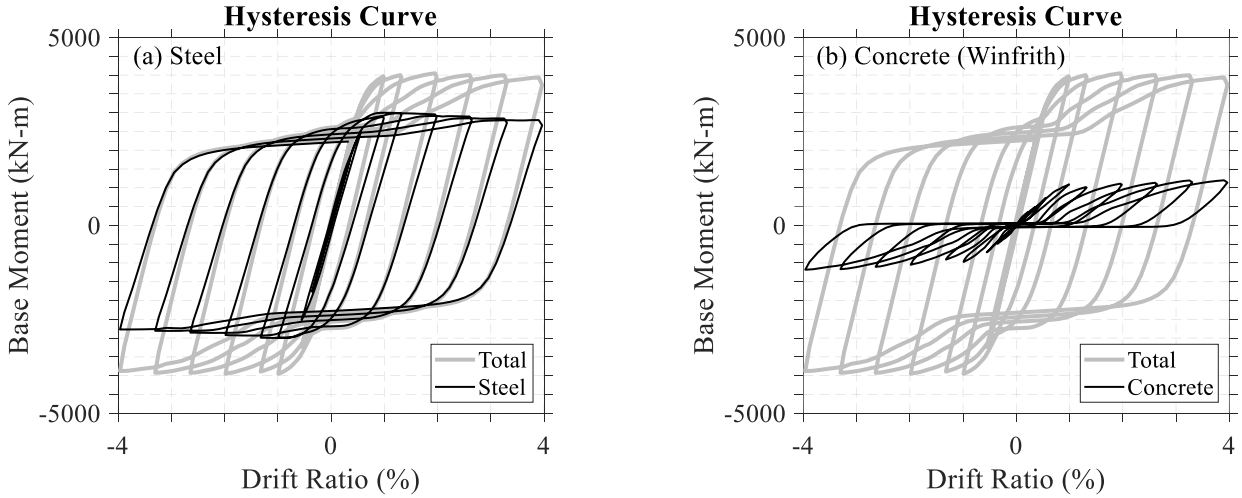

Fig. 6. Contribution of the wall parts to total base moment hysteresis of the wall with Winfrith (Mat085) concrete model: a) Steel; b) Concrete.

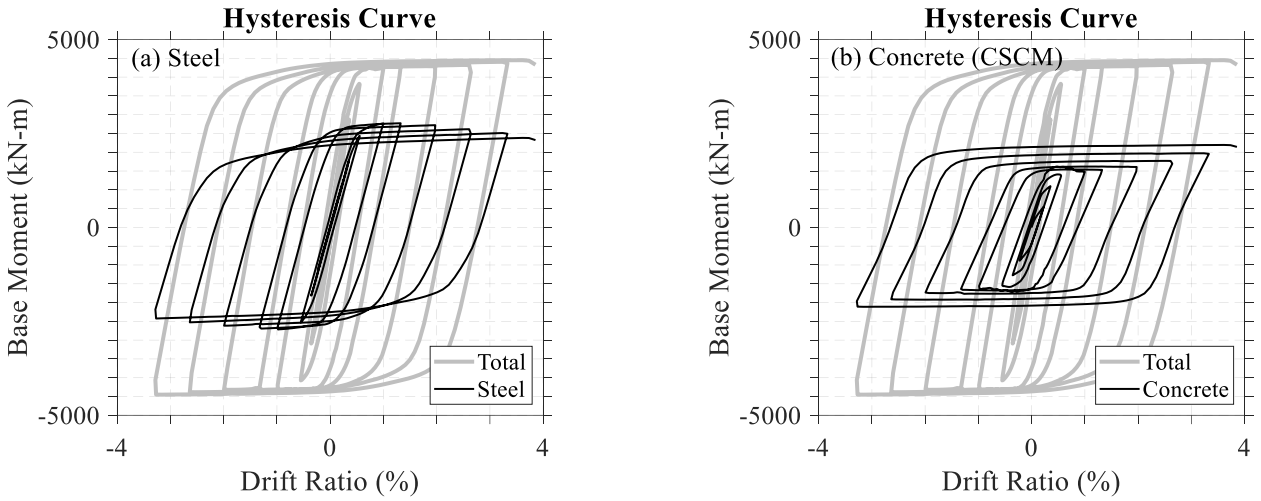

Fig. 7. Contribution of the wall parts to total base moment hysteresis of the wall with KCC (Mat072R3) concrete model: a) Steel; b) Concrete.

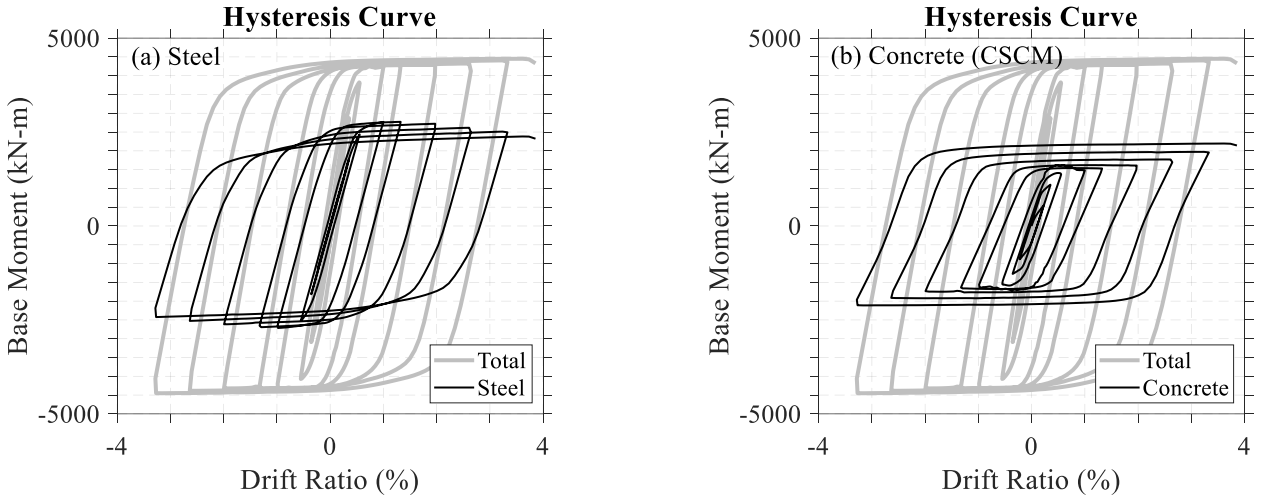

Fig. 8. Contribution of the wall parts to total base moment hysteresis of the wall with CSCM (Mat159) concrete model: a) Steel; b) Concrete.

7. Investigation of Moment Contribution of Wall Web and Boundary for Steel and Concrete

In flexural type shear walls, most of the moment demand is resisted by the boundary (outermost) region of the wall—while most of the shear force is mainly resisted by the wall web. The reference wall model under consideration has boundary elements in the form of full HSS and it is of interest to quantify individual contribution of the wall boundary and wall web regions of the steel and concrete parts to total base moment of the steel and concrete parts of the wall. In this section individual contribution of the steel web and steel boundary to total base moment of the total steel part (web and boundary), and contribution of concrete web and concrete boundary to total base moment of the total concrete part (web and boundary) of the wall were investigated for the walls using the three concrete models.

Figs 9-11 show the contribution of the wall steel (part (a) of the figures) and wall concrete (part (b) of the figures) to total base moment due to steel and concrete parts of the wall, respectively for the wall using the Winfrith, KCC and CSCM concrete material models. For all the walls with the three concrete material models considered, the steel boundary and the steel web account about 66% and 33% of the total moment contribution of the wall steel, respectively (i.e. at 2% drift ratio based on the results presented in part (a) of the figures). For the wall with the Winfrith concrete model, the concrete boundary and the concrete web account 74% and 26% of the total moment contribution of the wall concrete (per Fig. 9(b)). For the wall with the KCC concrete model, the concrete boundary and the concrete web account 97% and 3% of the total moment contribution of the wall concrete (per Fig. 10(b)). For the wall with the CSCM concrete model, the concrete boundary and the concrete web account 80% and 20% of the total moment contribution of the wall concrete (per Fig. 11(b)). Results indicate that for the wall with the KCC concrete, the concrete within the wall web has almost no contribution to wall moment. This indicates that neutral axis is close to the web-boundary interface region for this wall so that very little

amount of web concrete is under compression. For the wall with the Winfrith and CSCM concrete models, moment contribution of the web concrete is somewhat close to each other (26% vs. 20%). This indicates larger compression depth for these walls than obtained from the wall with KCC concrete model.

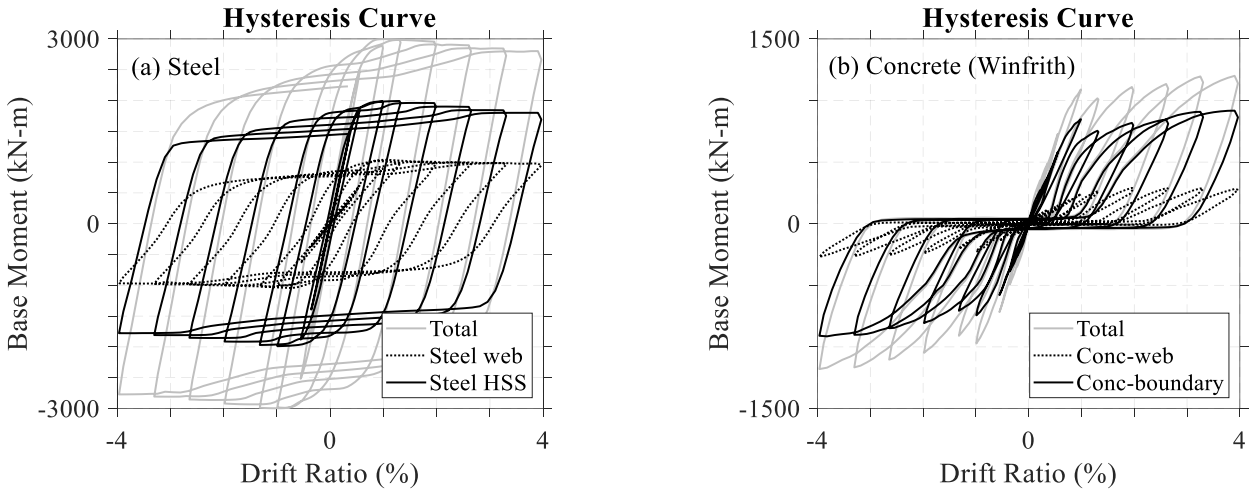

Fig. 9. Contribution of wall web and boundary elements to total base moment of the wall with Winfrith concrete model: a) Steel; b) Concrete.

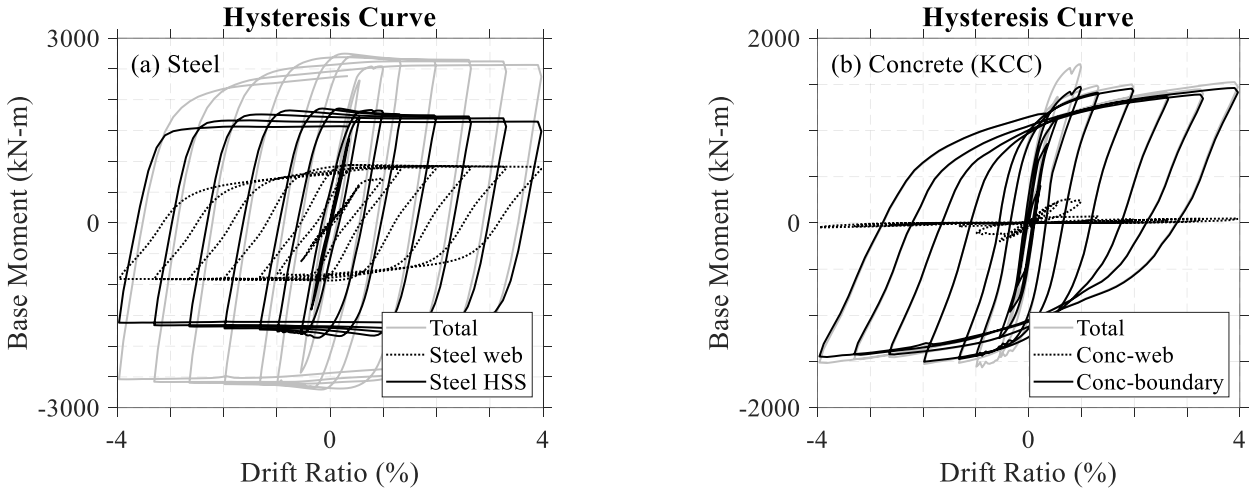

Fig. 10. Contribution of wall web and boundary elements to total base moment of the wall with KCC concrete model: a) Steel; b) Concrete.

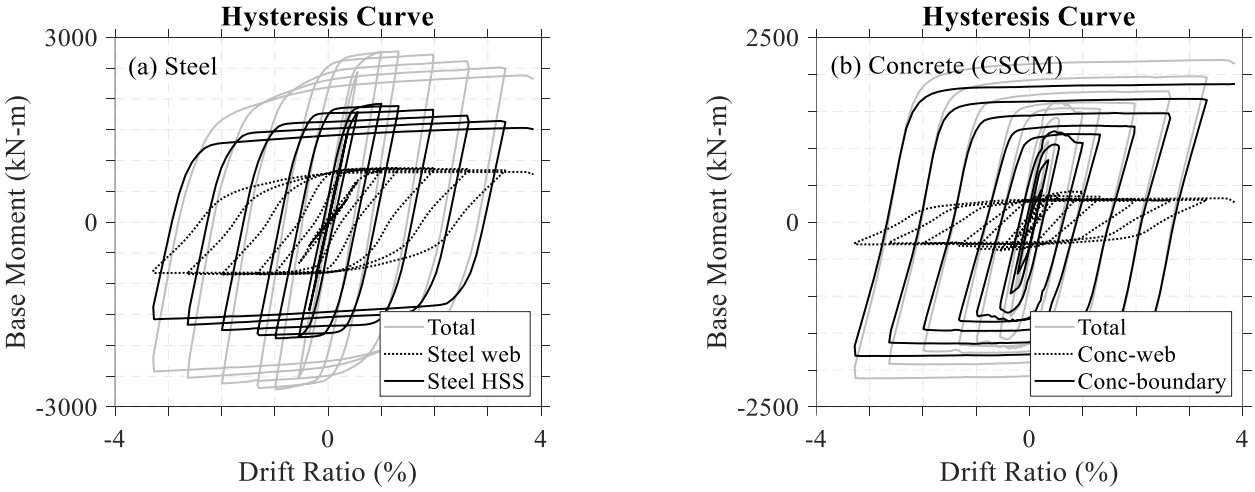

Fig. 11. Contribution of wall web and boundary elements to total base moment of the wall with CSCM concrete model: a) Steel; b) Concrete.

8. Comparison of Wall Neutral Axis and Concrete Axial Stress Distribution

Wall neutral axis obtained for the walls using the Winfrith, KCC and CSCM concrete models are compared. Axial stress contours of the infill concrete were plotted along the wall length at peak wall deformation for negative and positive values. This allowed comparison of the wall neutral axis, visually. For a quantitative comparison of the wall neutral axis and axial strength demand in the concrete, average axial stress distributions of the infill concrete at the wall base were obtained and plotted across the depth of the wall cross-section.

Fig. 12(a-c) shows negative and positive stress contours of the concrete of the walls using the Winfrith (a), KCC (b), and; CSCM (c) material models to show the wall neutral axis along the wall height. In this figure, compressive and tensile stresses are shown by two different colors (i.e., black and gray regions represent the compression and tension region of the wall, respectively). (Note that at larger drifts, the concrete under tensile stresses starts cracking – not shown in the figure – as such the compression depth is smaller than the half of the total depth). Focusing on the wall neutral axis at the wall base (highest axial strain region of the wall) the following observations can be made: the wall using the Winfrith concrete model exhibits slightly larger compression depth than that of the wall using KCC concrete model, and; slightly lower compression depth than that of the wall using CSCM concrete model.

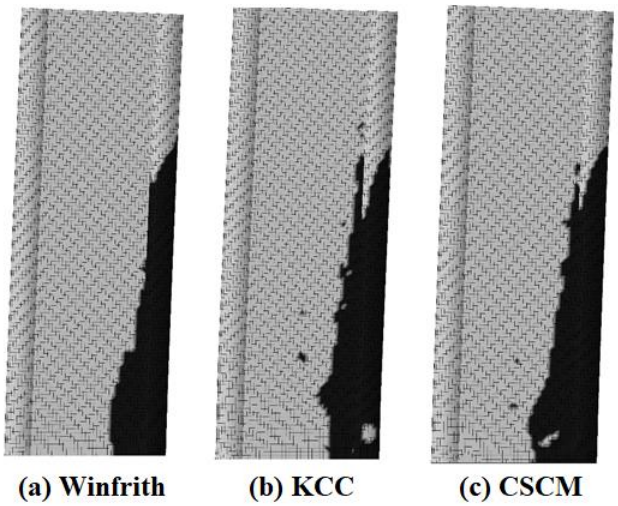

Fig. 12. Plastic neutral axis of the infill concrete of the walls with: a) Mat085, b) Mat072R3; c) Mat159.

Fig. 13 shows average axial stress distribution of the infill concrete obtained for wall using the Winfrith (a), KCC (b) and CSCM (c) concrete models at specified wall drifts of 0.25%, 0.5%, 1.0%, 1.5%, 2.0%, 2.5% and 3.0%. As shown in Fig. 13(a), for the wall with the Winfrith concrete model, maximum concrete strength was attained at the wall web. For example, the maximum average stress values of the concrete within the wall web is about 85MPa while the maximum averages stress values of the concrete core (inside the boundary element) is about 60MPa. The lower axial strength demand in the boundary element is attributed to possible slippage between the HSS and the concrete core (note that steel-concrete interaction of the boundary element is solely achieved by interface friction; i.e., no tie bars were used). As shown in Fig. 13(b), for the wall with the KCC concrete model, maximum concrete strength is attained at the wall boundary. For example, the value of the maximum average stress of the boundary concrete and web concrete are about 100MPa and 80MPa, respectively. As shown in Fig. 13(c), for the wall with the CSCM concrete model, maximum concrete strength is (similarly to the wall with the KCC concrete) attained at the boundary concrete having a maximum average stress of about 60MPa (note that, for this case, the average axial stress curves obtained are not as smooth as the curves obtained for the Winfrith and KCC concrete). Note that all the measured results exceed the unconfined uniaxial concrete compression strength of 49MPa which indicates some level of confinement of the concrete.

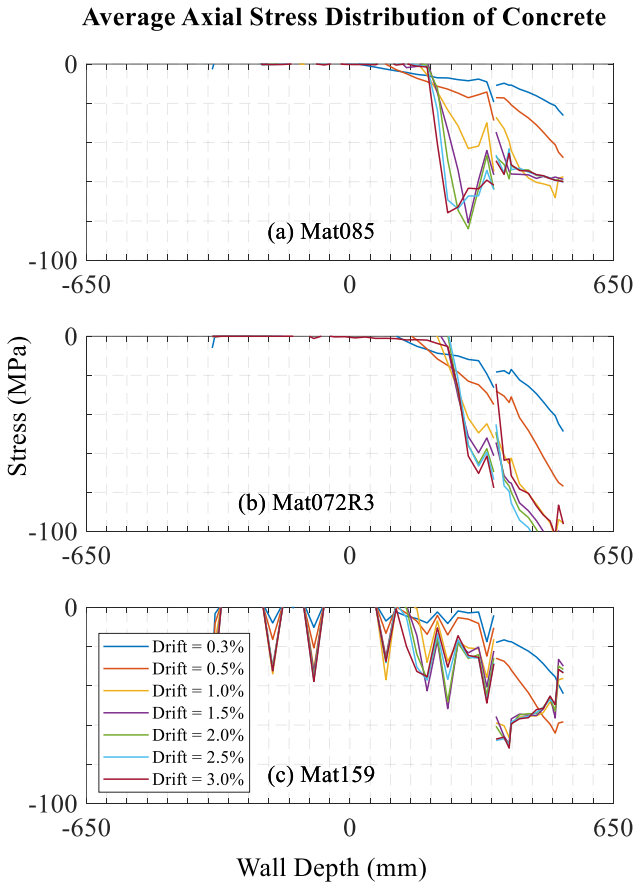

Fig. 13. Average axial stress distribution of concrete of the wall with: a) Mat085, b) Mat072R3; c) Mat159.

Fig. 13 reveals the compression depth of the wall models as a function of wall drifts. For example, it is shown that compression depth of the wall obtained using the Winfrith concrete model is slightly larger than that of the wall using the KCC concrete model, and lower than that of using the CSCM concrete model. From the figure, the predicted compression depth of the wall is about 350mm, 300mm and 450mm for the wall with the

Winfrith, KCC and CSCM concrete models, respectively. Recalling that the theoretically calculated plastic neutral axis was 360mm, the neutral axis, predicted by the numerical models, is less for the wall with KCC and higher for the wall with the CSCM concrete models.

9. Conclusions

Three concrete material models available in LS-Dyna, namely the Winfrith, KCC and CSCM, were used to investigate their influence on cyclic inelastic response of a previously benchmarked composite plates shear wall-concrete filled using LS-Dyna. Wall base moment hysteresis of the wall models using the three material models were obtained and compared. Results showed that wall lateral stiffness and strength prediction of the KCC concrete model was in good agreement with the previously benchmarked results for the wall using the Winfrith concrete model. Wall strength over-predicted by the CSCM concrete model. Both, the KCC and the CSCM concrete models could not capture the actual wall pinching.

Individual moment contributions of the steel and concrete showed for the wall with the KCC concrete model that, there is slight reduction in steel strength and slight increase in concrete strength with increasing wall drift. For the wall with the CSCM concrete model, the reduction in steel contribution and increase in concrete contribution with increasing wall drifts is more significant than that obtained using the Winfrith concrete model.

Investigation of moment contribution of wall web and boundary for steel and concrete showed for all the walls with the three concrete material models that, the steel boundary and the steel web account about 66% and 33% of the total moment contribution of the wall steel, respectively. On the other hand, contribution of the concrete web and concrete boundary to total moment contribution of the wall concrete varied for each of the concrete model used.

Investigation of wall neutral axis showed that, wall neutral axis obtained using the Winfrith concrete model is slightly larger than that obtained from the wall using the KCC concrete model and slightly smaller than that obtained from the wall using the CSCM concrete model. Average axial stress distribution of the concrete showed that maximum demand occurred at the wall web for the wall with the Winfrith concrete model; at the boundary element for the wall with the KCC and CSCM concrete models. For all the models, average axial stress values obtained were higher than the uniaxial unconfined compressive strength of the concrete, which indicated some level of confinement.

Publication Note

This research has previously been presented at the 8th International Symposium on Steel Structures held in Konya, Turkey, on October 25-26, 2019. Extended version of the research has been submitted to Challenge Journal of Structural Mechanics and has been peer-reviewed prior to the publication.

References

AISC (2016). Seismic provisions for structural steel buildings. *AISC 341-16*, AISC, Chicago.

Alzeni Y, Bruneau M (2017). In-plane cyclic testing of concrete-filled sandwich steel panel walls with and without boundary elements. *Journal of Structural Engineering*, 143(9), 04017115.

Epackachi S, Whittaker AS, Varma AH, Kurt EG (2015). Finite element modeling of steel-plate concrete composite wall piers. *Engineering Structures*, 100, 369-384.

Hibbett, Karlsson, Sorensen (2011). *ABAQUS/standard: User's Manual*. Dassault Systèmes Simulia, Providence, RI, USA.

Kurt EG, Varma AH, Booth P, Whittaker AS (2016). In-Plane behavior and design of rectangular SC wall piers without boundary elements. *Journal of Structural Engineering*, 04016026.

LSTC (2013). *Keyword User's Manual, Volume II, Material Models*, Livermore Software Technology Corporation (LSTC), Livermore, CA, USA.

Polat E, Bruneau M (2017). Modeling cyclic inelastic in-plane flexural behavior of concrete filled sandwich steel panel walls. *Engineering Structures*, 148, 63-80.

Polat E, Bruneau M (2018). Cyclic inelastic in-plane flexural behavior of concrete filled sandwich steel panel walls with different cross-section properties. *Engineering Journal, American Institute of Steel Construction*, 55, 45-76.

Varma AH, Shafaei S, Klemencic R (2019). Steel modules of composite plate shear walls: Behavior, stability, and design. *Thin-Walled Structures*, 145, 106384.